Department
Chemie und Pharmazie

FRIEDRICH-ALEXANDER
UNIVERSITÄT
ERLANGEN-NÜRNBERG
NATURWISSENSCHAFTLICHE
FAKULTÄT

Exploring Electron Beam Induced Processing with Metal-Organic and Organic Materials for the Fabrication of Hybrid Nanostructures

Untersuchung der elektronenstrahlinduzierten Effekte auf metallorganische und organische Materialen zur Herstellung von Nanohybridstrukturen

Der Naturwissenschaftlichen Fakultät der
Friedrich-Alexander-Universität Erlangen-Nürnberg

zur Erlangung des Doktorgrades Dr. rer. nat.

vorgelegt von

Christian Preischl

aus Ebermannsdorf

Als Dissertation genehmigt von der Naturwissenschaftlichen Fakultät der Friedrich-Alexander-Universität Erlangen-Nürnberg

Tag der mündlichen Prüfung: 21.07.2021

Vorsitzender des Promotionsorgans: Prof. Dr. Hans-Peter Steinrück

Gutachter: PD. Dr. Hubertus Marbach
Prof. Dr. Jörg Libuda

Table of Contents

Table of Contents

Published Papers

[P1] **Controlled Electron-Induced Fabrication of Metallic Nanostructures on 1nm Thick Membranes**

C. Preischl, L. H. Le, E. Bilgilisoy, F. Vollnhals, A. Gölzhäuser, H. Marbach

Small **2020**, *16*, 2003947; DOI: 10.1002/smll.202003947

The author´s contribution is the performance and interpretation of the EBID, AES, SAM, AFM and transfer experiments. The manuscript was prepared by the author.

[P2] **Exploring the Fabrication and Transfer Mechanism of Metallic Nanostructures on Carbon Nanomembranes via Focused Electron Beam Induced Processing**

C. Preischl, L. H. Le, E. Bilgilisoy, A. Gölzhäuser, H. Marbach

Beilstein J. Nanotechnol. **2021**, *12*, 319-329; DOI: 10.3762/bjnano.12.26

The author´s contribution is the performance and interpretation of the EBID, EBISA, AES, AFM and transfer experiments. The manuscript was prepared by the author.

[P3] **Ultrathin Carbon Nanomembranes from 5,10,15,20-Tetraphenylporphyrin: Electron Beam Induced Fabrication and Functionalization via Focused Electron Beam Induced Processing**

C. Preischl, M. Rohdenburg, E. Bilgilisoy, R. Cartaya, P. Swiderek, H. Marbach

J. Phys. Chem. C. **2020**, *124*, 28335-28344; DOI: 10.1021/acs.jpcc.0c09694

The author´s contribution is the performance and interpretation of the EBID, EBISA, AES and transfer experiments. The RAIRS and ESD data were acquired and analyzed together with M. Rohdenburg and R. Cartaya during a two-week research stay at the University Bremen. The manuscript was prepared by the author.

[P4] **Electron Beam-Induced Surface Activation of Metal-Organic Framework HKUST-1: Unravelling the Underlying Chemistry**

K. Ahlenhoff, **C. Preischl**, P. Swiderek, H. Marbach

J. Phys. Chem. C **2018**, *122*, 26658-26670; DOI: 10.1021/acs.jpcc.8b06226

The author´s contribution is the performance and interpretation of the EBID, EBISA and AES experiments. The manuscript was prepared in close cooperation by all authors.

1 Introduction

New technological trends such as artificial intelligence, internet of things and autonomous driving will have a huge impact on the future of mankind. All these technologies would not be possible without powerful and affordable hardware. This hardware is based on nanotechnology. Nanotechnology can be described as the production and characterization of structures with a size from 1 to 100 nm in at least one dimension. Modern semiconductor industry relies on nanotechnology and enables it to produce ever more powerful microchips with ever smaller structure sizes. The structures embedded in modern microchips are complex hybrids consisting of metals, semiconductors and insulating materials. The latest technology, which has reached production maturity, is the so-called extreme ultraviolet (EUV) lithography. This development allows that the predictions of Moore´s Law from 1965,[1] which states that the number of transistors in dense integrated circuits approximately doubles every two years, are still fulfilled.

In general, there are two different approaches for the production of nanostructures. The first one is the so-called bottom-up approach. Here, the effect of self-assembly of smaller entities, e.g., molecular building blocks or atoms, is used to create larger complex units. The second approach is the top-down approach, in which larger components are transformed into small devices by structuring techniques.[2] EUV lithography as well as standard ultraviolet (UV) lithography are typical top down approaches and consist of several complicated processing steps.

Another powerful top-down approach for the fabrication of nanostructures is focused electron beam induced processing (FEBIP),[3-5] which is the key method in this thesis. As the name implies, in FEBIP a focused electron beam is utilized to locally modify the properties of matter for the fabrication of well-defined, arbitrary shaped nanostructures. In the field of FEBIP, electron beam induced deposition (EBID) is the most investigated and prominent technique.[3-4, 6] In EBID, precursor molecules, which are usually metal–organic compounds, are decomposed by the impact of the electron beam such that ideally the nonvolatile metal center forms a deposit, whereas the volatile organic fragments desorb. In 2010, FEBIP was extended by a novel method referred to as electron beam induced surface activation (EBISA).[7-9] In EBISA, a surface is irradiated by a focused electron beam, resulting in an activation of the electron exposed areas.

Activation in that sense means, that the electron affected areas are chemically altered such, that a subsequently dosed precursor is decomposed at the latter sites. Thus, an "initial" deposit is formed. Under ultrahigh vacuum (UHV) conditions certain precursor molecules like $Fe(CO)_5$ and $Co(CO)_3NO$ tend to dissociate at these initial deposits and lead to an autocatalytic growth (AG). Using this effect, nanostructures with high purity and lower proximity effects can be fabricated.[9-13] So far, EBISA was conducted successfully with $Fe(CO)_5$ on silicon oxide,[8, 14] rutile $TiO_2(110)$,[11] surface-anchored metal-organic frameworks (SURMOFs),[15] and a thin layer of porphyrin molecules.[16-17] Whereas for $Co(CO)_3NO$ it was reported that EBISA only works on the electron beam activated areas of a thin layer of porphyrin molecules.[17] For oxide surfaces the activated sites have been identified as oxygen vacancies resulting from electron stimulated desorption (ESD).[11] In the case of organic and organometallic substrates, the nature of the activated sites and their formation has not yet been analyzed in detail. A part of the thesis at hand is therefore to gain insight in the molecular processes occurring on organic and metal-organic substrates during electron exposure.

A very-well studied organic system are self-assembled monolayers (SAMs), which can be fabricated via a wet-chemical bottom-up approach. SAMs consisting of aromatic molecules can be transformed into carbon nanomembranes (CNM) via electron or UV irradiation.[18] These CNMs are versatile two-dimensional (2D) materials with very high mechanical[19] and thermal[20] stability and tunable electrical conductivity and stiffness.[21] However, for several auspicious applications in optics (i.e. photonic and plasmonic devices), electronics (i.e. nanoelectromechanical systems (NEMS)[22]), and magnetics (i.e. switchable permeable membranes) further functionalization is necessary. In the thesis at hand a novel approach for the fabrication of complex hybrid structures consisting of metallic nanostructures on top of a 2D CNM is presented (cf. Chapter 3.1.1). Therefore, an aromatic SAM fabricated via a bottom-up process on a Au substrate is in a first step functionalized via a top-down method, i.e. EBID. After electron-induced cross-linking the functionalized CNMs were successfully transferred either onto solid SiO_2 substrate or onto grids to obtain free-standing metal/CNM hybrid structures. The iron structures on top of the 1 nm thick CNM stay intact during the whole process. In Chapter 3.1.2 this novel fabrication method is analyzed further by investigating different substrate materials for the growth of the SAM. EBID and EBISA were performed on a SAM grown on Ag with $Fe(CO)_5$ and $Co(CO)_3NO$. Here, the same trend as in previous results

occurs: EBISA is only working with $Fe(CO)_5$. Next to this, the EBISA process on SAMs shows a pronounced time dependence, which was never reported on other substrates before. Furthermore, the change of the substrate from Au to Ag and the associated change in the wet-chemical transfer process leads to shrinking and deformation of the iron structures and to dissolution of the cobalt-oxide structures during the transfer. Considering the huge variety of different precursor molecules available for FEBIP,[4] this result underlines the importance of studying the fabrication process and the interactions for different substrates, etching chemicals, and deposit materials.

In Chapter 3.2 the fabrication process is expanded to a different type of molecules for the fabrication of the 2D membrane. Instead of chemical bound aromatic SAMs, physisorbed porphyrin molecules are used. Porphyrins are key building blocks in nature[23-24] and due to their specific properties, they can also be used in several technical applications.[25-28] The resulting 1.5 nm thick CNMs consisting of cross-linked porphyrin molecules are stable throughout the whole transfer process and can even hold metallic iron structures on top without any support material. Furthermore, the processes occurring on a molecular scale during electron irradiation of the porphyrin molecules are analyzed via electron-stimulated desorption (ESD) and reflection absorption infrared spectroscopy (RAIRS).

In order to get further insight into the mechanisms of electron irradiation of organic respectively metal-organic materials a third type of substrate, namely surface-anchored metal-organic frameworks (SURMOFs) is investigated in Chapter 3.3. The well-studied SURMOF HKUST-1 is compared to surface-grown copper(II)-oxalate, regarding their selectivity in the EBISA process with the precursors $Fe(CO)_5$ and $Co(CO)_3NO$. EBISA was solely successful on the HKUST-1 sample with $Fe(CO)_5$. In the case of the copper(II)-oxalate sample EBISA worked with neither of the two precursors. Moreover, ESD and RAIRS were conducted on both substrates in order to study the molecular processes during electron irradiation. The results indicate that the aromatic building block, which is only present in the HKUST-1 plays a crucial role in the activation process for EBISA.

In summary the thesis at hand reports novel methods to fabricate complex hybrid nanostructures with high application potential via FEBIP methods.

2 Fundamentals and Techniques

2.1 Scanning Electron Microscopy (SEM)

In scanning electron microscopy (SEM) a highly focused electron beam is used to acquire images of a specimen surface down to sub-nanometer resolution. The highly focused electron beam (primary electrons, PEs) is scanned pixel by pixel across the surface. The energy of the PEs is determined by the acceleration voltage. The interaction of the PEs with the sample leads to the emission of electrons, which can be detected for image acquisition. Furthermore, X-rays and Auger electrons (AEs) are released, which can be employed for chemical analysis of the surface near region of the sample. A detailed introduction to scanning electron microscopy can be found in L. Reimer: "Scanning Electron Microscopy".[29]

In Figure 2-1 the so-called interaction volume of the PEs with the specimen is depicted. The most relevant interaction products are secondary electrons (SEs), backscattered electrons (BSEs), X-rays and AEs. The SEs (E_{kin} < 50 eV) and AEs (up to ~ 200 eV) are particularly surface-sensitive, i.e. they are emitted from the top-most surface layers (up to 10 nm[30]). However, the BSEs (E_{kin} > 200 eV) and X-rays are also emitted from below the surface (in the µm regime). The reason for this behavior is the difference in kinetic energy and the associated inelastic mean free path. SEs are generated by inelastic collision of electrons with sample atoms. Depending on the colliding electrons, they are divided into SE_I (for PEs) and SE_{II} (for BSEs). Instead of the SE_I, which contribute to the high resolution, the SE_{II} cause a background signal, as they are usually released farther away from the electron beam impact point due to their higher energies and thus larger mean free path. BSEs originate from multiple inelastic scattering of PEs. The diameter of the BSE exit area and the depth, which can both be well in the µm range, depends on the PE energy, the sample properties such as density and the atomic numbers. The generation of characteristic X-rays and AEs is a complementary process. The photons (i.e. X-rays), as well as the AEs obtain a characteristic element specific energy, almost like an elemental fingerprint, which can be used for chemical analysis of the specimen.

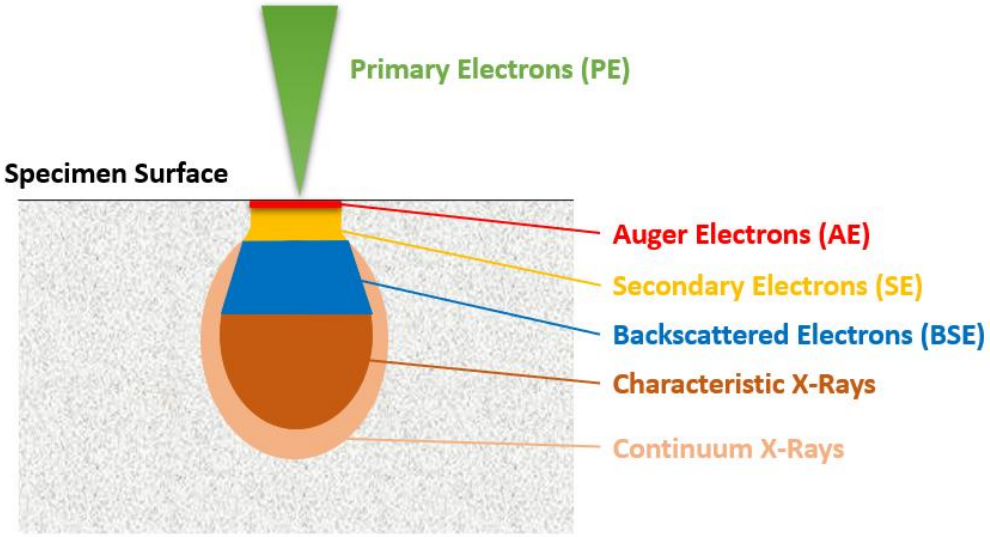

Figure 2-1: Interaction volume of the impinging primary electron beam with the specimen and regions from which the different signals originate.[29]

In a SEM, the signals measured by the detector are deployed for image formation. The most commonly used detectors are SE detectors, like the well-known "Everhart-Thornley detector".[31] For imaging, the SEM technique relies on different types of contrast mechanisms. Generally, there are two major types of contrast mechanisms.

The first one is the so-called topographical contrast and yields a three-dimensional impression of the surface topography in the SEM image. Several effects like surface-tilt contrast, shadowing contrast, edge effect and surface-roughness contrast can be subsumed under the topographical contrast mechanisms. A tilted surface leads, due to smaller escape depths, to a higher electron emission and thereby to a brighter SEM image. The shadowing contrast appears when the signal path to the detector is blocked by surface features. For structures with a large available surface for emission such as edges and rough i.e., edge-rich surfaces the electron emission is increased. Micro-rough surfaces appear brighter than flat surfaces of the same material.[29]

The second type of contrast mechanism is the material-based contrast. The material contrast depends on the chemical and physical properties like mean atomic number Z, density, atomic order, possibly crystal orientation and electric and magnetic properties of the surface. The most important material contrast is the chemical contrast. With an increasing atomic number Z the BSE emission coefficient increases. From this follows that a metal appears brighter in SEM compared to organic or carbon covered surfaces.[29]

2.2 Auger Electron Spectroscopy (AES)

Auger electron spectroscopy (AES) is a powerful technique for the qualitative and quantitative chemical analysis of specimen surfaces. As low energetic AEs are emitted from the top-most surface layer, AES is a surface-sensitive method. A focused electron beam utilized as excitation source enables to perform local AES and scanning auger electron microscopy.

AES is based on the Auger emission process, which is indicated in Figure 2-2: An incident electron with a sufficient high energy can excite inner shell electrons (in this example K shell) of surface atoms, resulting in an inner shell vacancy. This inner shell vacancy is referred to as core hole. The atom is ionized and therefore in an excited state. The relaxation from excited to ground state occurs by filling the vacancy with an electron from a higher-level energetic shell (here L_1 level). The released energy can either be transferred to another electron (here $L_{2,3}$ level), which is ejected from the atom as AE, or the gained energy is emitted as X-ray photon.[32]

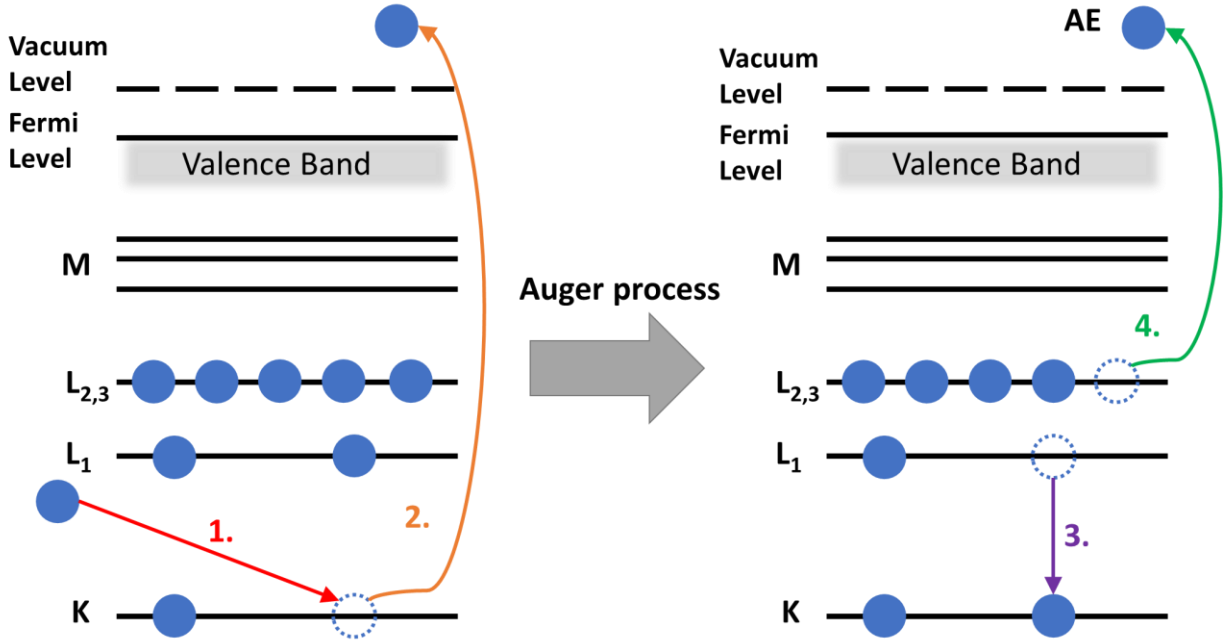

Figure 2-2: Schematic description of the Auger process. 1. and 2. A K-shell electron is ejected by the incident radiation, creating a vacancy. 3. An electron from an outer shell (L1) fills the hole, releasing energy. 4. The released energy is transferred to another electron (L2,3), which is then emitted as the Auger electron.[32]

Note that the energy of the emitted AEs only depends on the energetic states of the shells of the involved atom. Thus, the energy of the released AE is independent of the primary electron energy. The following equation estimates the approximated energy of the AE relative to the Fermi level. This model is simplified as it does not consider the interaction between the core holes neither the relaxation energies resulting from the core screening.

$$E_{KL_1L_{2,3}} = E_K - E_{L_1} - E_{L_{2,3}}$$

E_K, E_{L1} and $E_{L2,3}$ represent the binding energy of the involved shells. The nomenclature for Auger emission processes is defined as the following. The first letter describes the shell of the core hole (i.e.: K), the second one the shell of the electron (i.e.: L_1), which fills the core hole and the third one represents the shell of the electron that is emitted (i.e.: $L_{2,3}$). In this example, the auger transition would be called $KL_1L_{2,3}$ or short KLL.

2.3 Quadrupole Mass Spectrometry (QMS)

The chemical composition of molecules in the gas phase can be analyzed via quadrupole mass spectrometry (QMS). Thereby, the molecules are ionized and the resulting charged fragments are separated according to their mass to charge ratio m/z by a corresponding filter. A suitable detector, which can either be a faraday cup or a secondary electron multiplier detects the incoming charged fragments.[33] The ionization of the molecules is realized via electron impact (EI) ionization. The filter for ion separation in a QMS is based on four parallel metal rods (quadrupole). On these rods a high frequency alternating electrical field, which is superimposed with a direct current (DC) voltage, is applied. Ions with a certain mass-to-charge ratio m/z can only reach the detector at a specific voltage ratio. For all other voltage ratios the same ions have an instable trajectory and do not reach the detector.[34]

In this thesis QMS was used for the analysis of residual gas composition, purity inspection of the precursors $Fe(CO)_5$ and $Co(CO)_3NO$ and for detection of fragments formed during electron irradiation of different substrates (i.e. ESD).

2.4 Atomic Force Microscopy (AFM)

Atomic force microscopy (AFM) is a scanning probe technique that enables monitoring the surface topography down to the atomic scale.[35] A sharp tip mounted on a cantilever is raster-scanned over the surface. At each point of the surface various tip-sample interactions occur. A distinction is made between short-range and long-range forces. The short-range forces are dipole-dipole interaction forces and friction forces, whereas the long-range forces are van der Waals forces, capillary forces (only in air) and electrostatic forces. Generally, the different forces cause a response of the cantilever-tip system which can be used for image formation. For example, these forces cause a vertical deflection of the cantilever, which can be measured by a deflection sensor. The deflection sensor (e.g. reflection of a laser beam from the cantilever) is utilized to generate an image of the surface topography.[36-37]

With AFM the surface topography can be determined with very high resolution. In addition, AFM can be performed on all solid types of surfaces regardless of the conductivity of the sample. Different operation modes can be used for AFM measurements. The most important operation modes are the contact mode (static mode), the non-contact mode (dynamic mode) and the tapping mode (dynamic mode).[36] In this work AFM was performed by using the tapping mode. In tapping mode (also referred to as intermittent mode), the cantilever is oscillating close to its resonance frequency. The tip "slightly" taps the surface of the sample during scanning. As the tip approaches the sample, the tip-sample interactions alter the amplitude, resonance frequency, and phase angle of the oscillating cantilever. A constant oscillation amplitude at the operating frequency is achieved by adjusting the position of the tip with respect to the sample.[38]

2.5 UHV Instrument

Most experiments presented in the thesis at hand were performed in a modified commercial UHV system (MULTISCAN Lab, Omicron Nanotechnology, Germany) with a base pressure of 2×10^{-10} mbar (see Figure 2-3). The system consists of two main chambers for analysis (analysis chamber) and sample preparation (preparation chamber) and two auxiliary chambers for sample transfer (fast entry lock) and precursor gas handling (gas dosing chamber).

The system is described in detail in the doctoral theses of Thomas Lukasczyk[39] and Michael Schirmer.[40] In the following the most important aspects of the system relevant for the thesis at hand are summarized

The main part of the analysis chamber is a UHV compatible electron column (Leo Gemini) which is utilized together with the Inlens detector for scanning electron microscopy (nominal resolution better than 3 nm). The hemispherical energy analyzer (Nano SAM EA U7 analyzer, Omicron) allows AES and scanning Auger microscopy with an ultimate resolution < 10 nm. The gas dosing chamber is connected with the analysis chamber via leak valves. For FEBIP experiments the precursor is supplied via a gas dosing nozzle (inner diameter 3 mm) with an adjustable distance towards the stage. In all FEBIP experiments, the distance between the end of the nozzle and the stage was adjusted to approximately 12 mm. The local pressure of the precursor at the sample surface is thereby enhanced by a factor of 30 (9.0×10^{-6} mbar)[40-41] as compared to the nominal background pressure of 3.0×10^{-7} mbar which was adjusted for all FEBIP experiments. The analysis chamber and the gas dosing chamber are both equipped with a QMS (Prisma QME 200, Pfeiffer) for precursor quality and residual gas control.

The preparation chamber is equipped with a QMS (Prisma QME 200, Pfeiffer), a quartz crystal micro balance (OSC-100A, Syscon), self-constructed Knudsen cell evaporator for organic materials, a sputter gun (ISE 10, Omicron), an electron flood gun (Flood Source FS 40A1, Prevac) and leak valves. The attached fast entry lock enables the introduction of samples without breaking the vacuum. A manipulator allows several different heating options (resistive, radiative, electron bombardment) depending on the used sample holder.

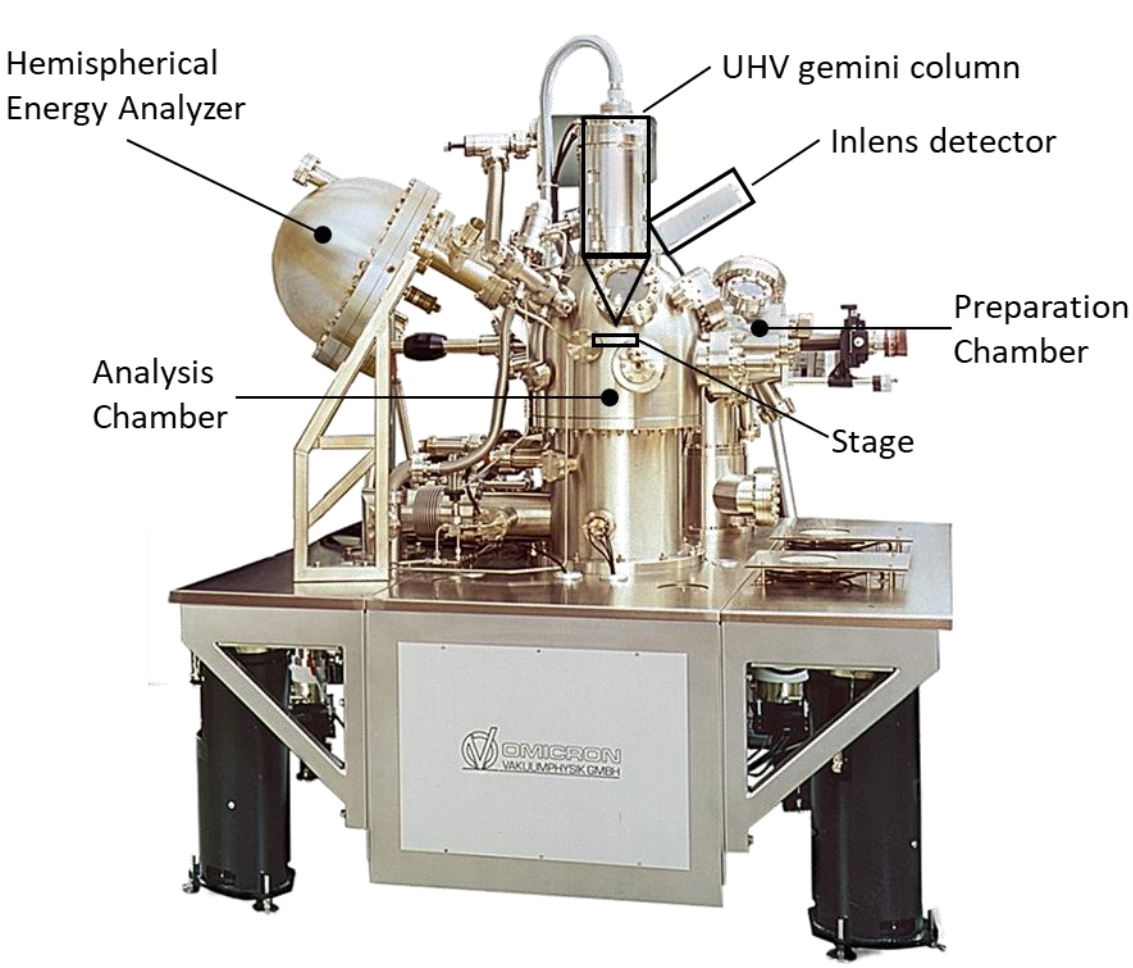

Figure 2-3: Image of the UHV system without gas dosing chamber, gas dosing nozzle and cable connections. The main parts are highlighted.

2.6 Samples and Precursors

2.6.1 Self-Assembled-Monolayers (SAMs) & Carbon Nanomembranes (CNMs)

A SAM is a system in which organic molecules from the liquid or gas phase spontaneously adsorb onto a solid surface and organize in a crystalline or semicrystalline structure (bottom-up approach). Usually, the organic molecules are composed of a "tailgroup" and a "headgroup", whereby the latter exhibits a certain chemical functionality.[42] The spontaneous formation of a SAM is driven by the strong binding affinity of the headgroup towards the substrate surface. For metals, metal oxides and semiconductors several different headgroups are available.[42] The probably best studied headgroup are thiols. Thiols show a strong affinity towards gold,[43-47] silver,[48-49] copper,[50] palladium[51-52] and platinum[53] and can be used to form well-defined organic surfaces. The thiols form a strong surface bond e.g., a metal thiolate, with the substrate surface (chemisorption). Furthermore, the intermolecular, e.g. van der Waals, interactions between the organic molecules additionally stabilize the SAM.[42] In this thesis SAMs formed from the aromatic molecule terphenylthiol (TPT) (see Figure 2-4), which have been prepared by the group of Prof. Dr. Gölzhäuser from the University of Bielefeld, are investigated.

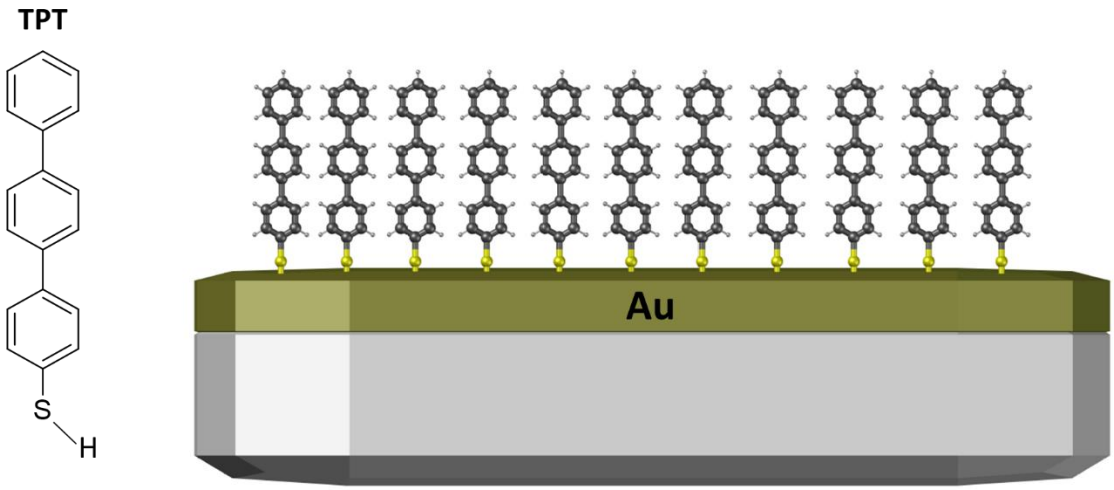

Figure 2-4: Chemical structure of the molecule terphenylthiol (TPT) and a schematic of a SAM of TPT on a Au substrate.

SAMs are 2D nanostructures with useful properties for several applications. Metallic surfaces like copper can be protected from oxidation by coating with a SAM.[54] Next to this the wetting and adhesion properties of surfaces can be modified.[50] Due to the well-ordered surface SAMs can be used as a starting point for the growth of SURMOFs (see Chapter 2.6.3).[55] A chemisorbed SAM changes the work function of the corresponding metal.[56] Therefore, SAMs are outstanding candidates for the fabrication of electronic devices, like organic field effect transistors.[57-60] Another important property of SAMs is that they can be patterned in the nanometer scale by either microcontact printing,[61-62] photon irradiation[63-65] or electron irradiation.[66-68]

Electron irradiation of SAMs induces the cleavage of C-H bonds and a lateral cross-linking of neighboring molecules.[18, 69] This cross-linking process leads to the formation of a 2D carbon nanomembrane (CNM).[70] CNMs obtain a high thermal[20] and mechanical[19] stability. The properties like conductivity, stiffness, thickness and porosity of the CNM are tunable as they are determined by the utilized SAM.[21, 71] Furthermore, CNMs can be lift-off from the substrate and transferred to arbitrary substrates and porous grids to obtain free-standing 2D CNMs. It was reported that CNMs with sub-nm pores can separate ions from water during osmosis.[72] Freestanding CNMs can also be used as mechanically stable nonconductive support for metallic structures fabricated via electron beam lithography (EBL).[73] Such hybrid materials are promising candidates for the fabrication of nanoelectromechanical systems (NEMS)[22] or photonic and plasmonic devices.[74] In this thesis, by using FEBIP, a new method for the fabrication of hybrid structures consisting of metallic nanostructures on top of 2D CNMs is successfully explored. Furthermore, fundamental studies about EBID and EBISA on a SAM of TPT molecules are presented.

2.6.2 Porphyrins

The characteristic chemical structure of porphyrins is a macrocycle consisting of four pyrrole rings linked by four methine bridges.[75] The basic porphyrin is porphin (see Figure 2-5). Attachment of substituents towards different positions on the macrocycle allows the fabrication of a huge variety of different porphyrins with tailored properties.[76] In Figure 2-5 the 5,10,15,20-

Tetraphenylporphyrin (2H-TPP) is depicted. To illustrate the versatile functionality of porphyrins two prominent examples from biological systems in nature are briefly discussed. The functionality of the heme complex in, e.g., human blood, is based on an iron(II)-porphyrin which effectively enables the oxygen transport in the blood stream of mammals.[75] A second prominent example is chlorophyll A, which main functional building block is a magnesium(II)-porphyrin. Chlorophyll A is responsible for the electron transfer during photosynthesis.[75] In addition, porphyrins have also been used in several technical applications like catalysis,[28] sensors,[26] or dye-sensitized solar cells.[27] Thin layers of porphyrins on metals and metal oxides can be prepared in a bottom-up approach by physical vapor deposition and the adsorption behavior has intensively been studied.[77-80]

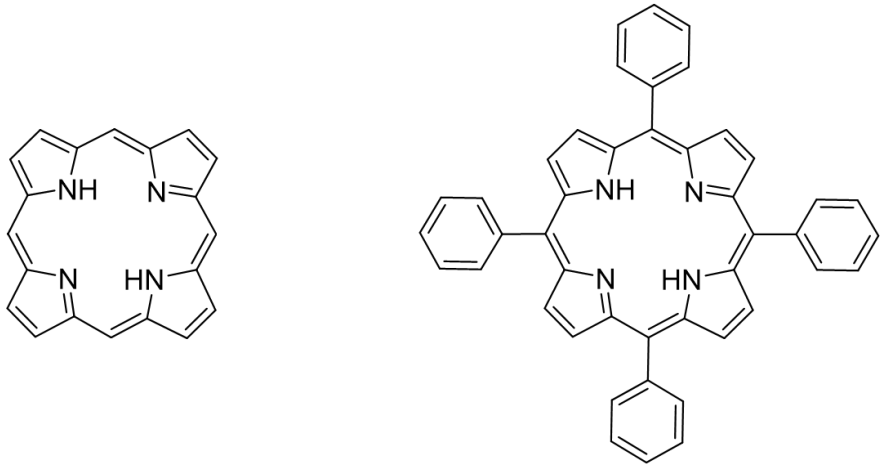

Porphin 2H-Tetraphenylporphyrin; 2H-TPP

Figure 2-5: The chemical structure of porphin and 2H-TPP

Ultrathin layers of 2H-TPP have already been investigated in terms of FEBIP.[16-17] They drastically reduce proximity effects and EBISA was conducted successfully with $Fe(CO)_5$ and $Co(CO)_3NO$.[17] However, the nature of the active sites that causes the decomposition of the precursors is still not fully understood. Within this thesis the electron induced effects occurring on a molecular scale on 2H-TPP are investigated and discussed. Furthermore, a new type of stable CNMs is presented, which can be prepared from thin layers of 2H-TPP molecules via electron induced cross-linking.

2.6.3 Surface-Anchored Metal-Organic Frameworks (SURMOFs)

A metal-organic framework (MOF)[81-82] which is epitaxially grown on a surface is referred to as surface-anchored metal-organic framework (SURMOF).[83] The highly porous three-dimensional (3D) framework is built via the coupling of metal ions with organic linker molecules. The variation of the building blocks enables the fabrication of a huge variety of SURMOFs with different properties like pore size, orientation and density.[81, 84-85] MOFs are versatile materials and can be used in several applications like gas storage,[85] drug release[86-87] and separation.[88-89] Furthermore, MOFs with embedded metal nanoparticles are an interesting class of material for catalysis and sensor technology.[90-92] A SURMOF is usually fabricated in a controlled layer-by-layer fashion by alternatively dipping the substrate into separate solutions containing the metal ion respective to the organic linker. As already mentioned in Chapter 2.6.1 SAMs are suitable starting substrates for the controlled fabrication of SURMOFs.[55]

A recent work from Drost et al. reports about FEBIP on the SURMOF copper benzene-1,3,5-tricarboxylate (HKUST-1).[15] HKUST-1 is a well-studied MOF consisting of the organic linker molecule benzene-1,3,5-tricarboxylate (btc) which coordinates copper(II) ions (see Figure 2-6).[93] In the latter study it was demonstrated that SURMOFs, due to reduced proximity effects, are suitable substrates for the fabrication of sub-10 nm structures via EBID. Furthermore, it was reported that EBISA is possible on HKUST-1 with $Fe(CO)_5$, whereas EBISA did not work with $Co(CO)_3NO$ on the same substrate.[15]

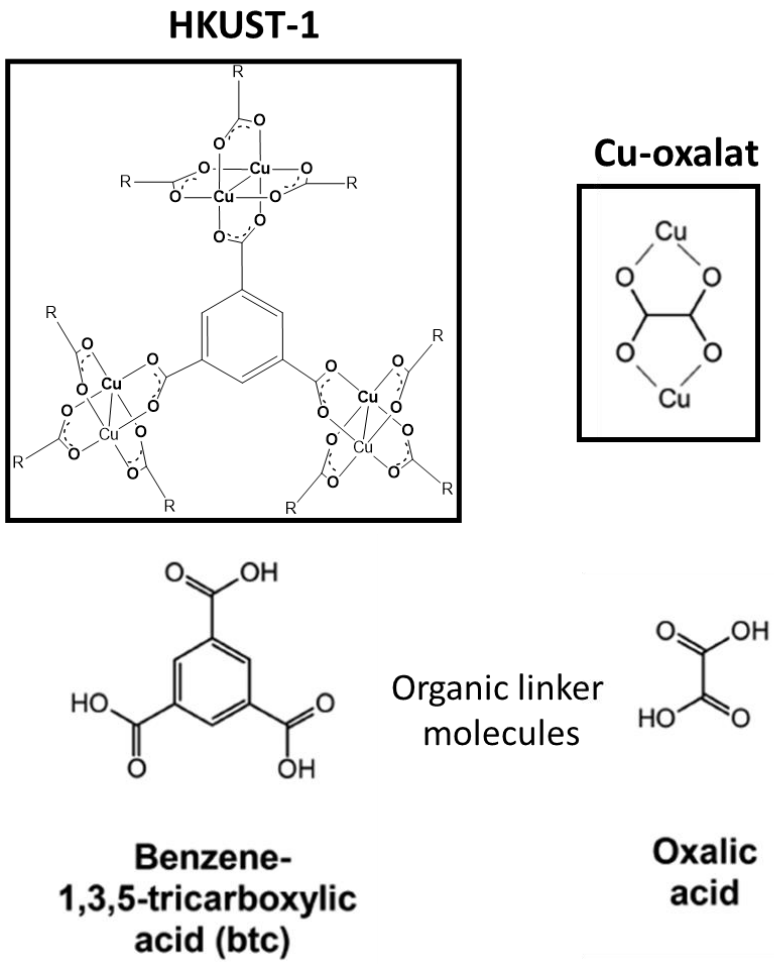

Figure 2-6: The MOF HKUST-1 and the corresponding linker molecule benzene-1,3,5-tricarboxylic acid (btc). Copper(II)-oxalate and the organic linker molecule oxalic acid.

Within the thesis at hand the EBISA process and especially the active species of the SURMOF HKUST-1 is further analyzed. Therefore, a HKUST-1 and a surface grown copper(II)-oxalate (see Figure 2-6) were prepared in the same layer-by-layer approach within a collaboration with the group of Prof. Swiderek from the University Bremen. By following this approach, only the organic linker molecule is varied. Both substrates were investigated regarding EBID and EBISA with the precursors $Fe(CO)_5$ and $Co(CO)_3NO$. Furthermore, the electron induced effects on both substrates were investigated via AES, ESD, and RAIRS.

2.6.4 $Fe(CO)_5$

Iron pentacarbonyl ($Fe(CO)_5$ see Figure 2-7) was purchased from ACROS Organics with a specified purity of 99.5 %. $Fe(CO)_5$ is an orange liquid which is sensitive towards air and UV irradiation. Therefore, the precursor was filled under inert gas conditions and stored in a glass/stainless steel container covered with aluminum foil. Before each FEBIP experiment, the stainless steel line for the precursor supply was purged several times with $Fe(CO)_5$. The quality of the precursor gas was analyzed with a quadrupole mass spectrometer in a dedicated gas analysis chamber (base pressure 2×10^{-9} mbar). For successful AG, a peak intensity ratio of Fe/CO (m/z = 56 vs. m/z = 28) of at least 0.05 is required.

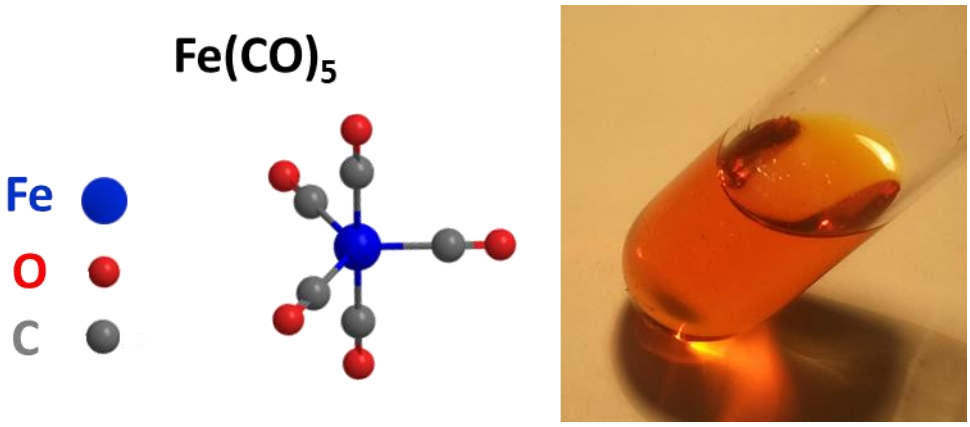

Figure 2-7: The precursor $Fe(CO)_5$.

2.6.5 $Co(CO)_3NO$

Cobalt tricarbonyl nitrosyl ($Co(CO)_3NO$ see Figure 2-8) was purchased from abcr GmbH & Co. KG. $Co(CO)_3NO$ is a dark brown liquid and was handled the same way as $Fe(CO)_5$ due to air and light sensitivity. For this precursor, the peak intensity ratio of Co/CO (m/z = 59 vs. m/z = 28) was analyzed in order to control the precursor purity. A ratio of at least 0.15 was required to observe pronounced AG.

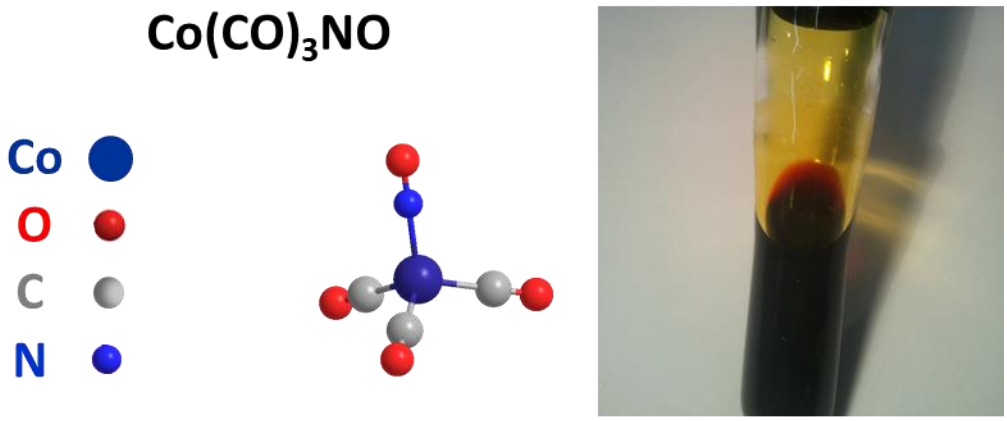

Figure 2-8: The precursor $Co(CO)_3NO$.

2.7 Electron Beam Induced Lithographic Techniques

In this Chapter, a brief introduction to the two investigated focused electron beam induced fabrication (FEBIP) methods is given. The two methods which are part of this thesis are EBID and EBISA. For the analyzed precursor molecules $Fe(CO)_5$ and $Co(CO)_3NO$ the autocatalytic growth (AG) process plays a crucial role and is therefore also part of this Chapter.

2.7.1 Electron Beam Induced Deposition (EBID)

Electron beam induced deposition (EBID) is a powerful direct-write method for the controlled fabrication of nanostructures.[3-4] The discovery of this novel method dates back to 1934, as it was reported that a carbonaceous layer is formed when the residual gases inside the SEM chamber are dissociated by the influence of the electron beam.[94] This effect was rendered as not useful for a long time as it was considered solely as a contamination. In the 1960s, this phenomenon was exploited for the first time to create metallic films via EBID of organometallic precursor molecules.[95] Since then, numerous works on EBID have been carried out and a significant progress has been achieved. For the interested reader, several review articles are available.[3-5, 96-97]

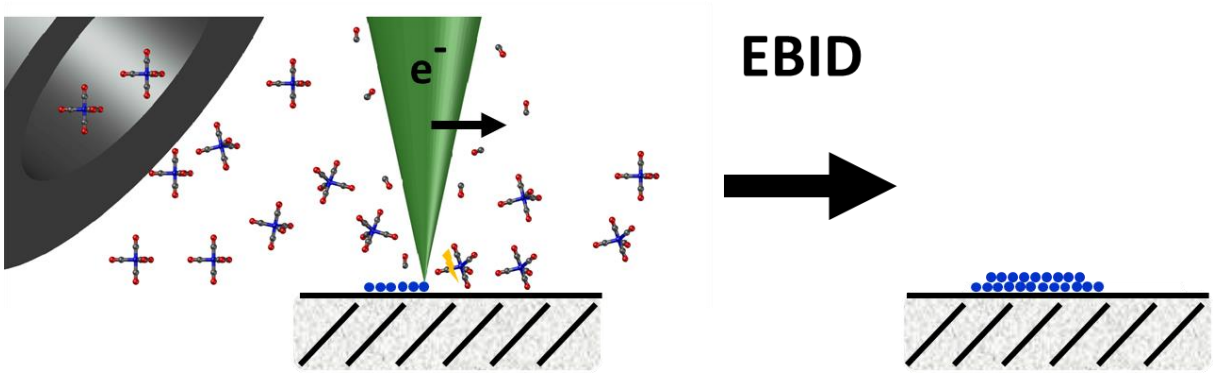

Figure 2-9: Scheme of the idealized EBID process. The precursor molecules are supplied via a nozzle and adsorb onto the surface. The adsorbed precursor molecules are dissociated via the focused electron beam. The non-volatile metallic fragments form the nanostructure while the volatile organic fragments are pumped off.

The EBID process is schematically depicted in Figure 2-9. Metal-organic precursor molecules are supplied via a thin nozzle which is in close proximity to the substrate surface. The usually gaseous molecules adsorb onto the substrate surface. A focused electron beam, e.g., of a SEM, is raster-scanned with lithographic control over the surface and induces the dissociation of the adsorbed precursor molecules via the impact of the PEs and the fabrication of BSEs and SEs with the latter. Ideally, the non-volatile metallic fragments remain at the point of impact and form the deposit, whereas the volatile fragments are pumped away. Compared to classical EBL, EBID possesses the advantage to fabricate nanostructures within one processing step. The fabrication of more complex and 3D nanostructures is also feasible via EBID.[98-99] Furthermore, a huge variety of different precursor molecules is available which enables the production of different metallic nanostructures.[4] Numerous interesting applications have already been realized with the use of EBID. Qian et al. showed that highly stable and sensitive AFM tips can be fabricated via EBID.[100-101] Furthermore, Pt field emitter and nanowires can be realized by performing EBID with the precursor $C_5H_5Pt(CH_3)_3$.[102-103] In the semiconductor industry, EBID has become one state-of-the-art method for repairing masks for UV and EUV lithography.[104-105] Combined with electron beam induced etching (EBIE) all types of nanoscale defects on masks can be targeted for repair.

Major challenges in EBID are the realization of desired elemental composition/purity of the deposit, the undesired broadening of the deposit caused by proximity effects and the rather low deposition rate.[3]

EBID is mainly used in high vacuum (HV) setups and most precursors yield depositions with purities most significantly lower than 60 at%.[106] The impurities in a high vacuum setup can be caused by adsorbed residual gas molecules (e.g. hydrocarbons), which are decomposed by the electron beam and thus incorporated in the deposit, or by non-volatile precursor fragments, which typically contain carbon, oxygen or nitrogen. Nevertheless, there are some exceptions, which show a higher purity. With the precursor $Co_2(CO)_8$, Co nanowires with a purity up to 95 at% can be realized.[107] Silver structures with a purity up to 76 at% can be fabricated with the precursor $AgO_2CC_2F_5$.[108] The problem of low purity deposition induced the development of several post-treatment cleaning procedures.[106, 109-114] One example for these cleaning procedures is the combination of EBID with a simultaneous water dosage for the fabrication of Au nanostructures with a purity up to 91 at%.[115] Recently we demonstrated in our group in Erlangen that by improving the vacuum conditions from high vacuum to UHV it is possible to fabricate iron nanostructures with ultra-high purity (≥ 95 at%) via EBID followed by AG (see Chapter 2.7.3).[12-15] In addition UHV allows to investigate FEBIP with significantly reduced residual gases and thus better defined conditions than in HV experiments. In the thesis at hand, all EBID experiments are performed under UHV conditions in order to achieve deposits with higher purity and to study the processes in a "surface science" fashion.

The smallest reported feature size reported so far within EBID was even below 1 nm.[116] Nevertheless, feature sizes in the sub 10 nanometer regime are challenging among others because proximity effects cause undesired co-deposition and thus broadening of the feature size.[3] The impinging electron beam leads to the formation of BSEs and SEs with a radial symmetry distribution up to several µm around the point of impact. This distribution radius strongly depends on the substrate material and can be predicted for BSEs via Monte-Carlo simulation. The BSE proximity effect occurs when BSEs and the induced SEs cross the interface between surface and vacuum in the proximity of the impact point and potentially dissociate adsorbed precursor molecules. Another dominant proximity effect occurring during EBID is caused by forward scattering. In forward scattering the PE beam scatters on pre-deposited material and yields forward scattered electrons (FSE). These FSEs can also induce the dissociation of adsorbed precursor molecules in the proximity of the impact point.

BSEs and SEs exhibit a wide range of kinetic energies from > 0 eV up to the primary beam energy. Therefore, the precursor molecules can be dissociated in several different

dissociation mechanisms which are listed in the following.[117] The probability for the scission of a bond in the precursor molecule strongly depends on the energy of the impinging electron and is generally expressed as a cross-section.[3] Dissociative Ionization (DI) with the highest cross section between 70 and 100 eV is caused by PEs, BSEs and FSEs.[4] The highest cross-section for the dissociation into neutrals (ND) is around 50 eV.[4] Dissociative electron attachment (DEA), which is the main pathway for the dissociation of precursor molecules by SEs, only occurs at a few eV within a narrow range.[117] As all these dissociation pathways occur more likely at energies below 100 eV it is supposed that corresponding " low-energetic electrons" are far more efficient for precursor dissociation than the PEs. Nevertheless, the contribution of the PEs should not be neglected as the high current density might antagonize the low cross-section. Most cross-section measurements for EBID precursors were performed in gas-phase studies.[118-120] However, in EBID these cross-sections might differ as the interplay with the surface needs to be considered as well.[121-122] Within the last decade several studies addressing the electron induced dissociation mechanisms of adsorbed EBID precursor were performed.[123-127]

2.7.2 Electron Beam Induced Surface Activation (EBISA)

The second FEBIP method investigated in this thesis was introduced in 2010 by Walz et al. and is referred to as electron beam induced surface activation (EBISA).[8] The EBISA process is schematically depicted in Figure 2-10. In a first step a suitable surface is irradiated with the focused electron beam under vacuum conditions e.g., no precursor is present. This electron irradiation induces a local chemical modification/activation of the surface such that it becomes catalytically active toward the decomposition of subsequently dosed precursor molecules. Consequently, in the second step, the surface is exposed to the precursor gas, which reacts with the pre-irradiated active areas. This reaction causes the dissociation of the precursor molecules and the non-volatile fragments form a first deposition layer. Upon further precursor dosage this first deposition layer can be converted into the desired deposit by AG (see Chapter 2.7.3). A detailed description of EBISA can be found in a review paper by Marbach.[7]

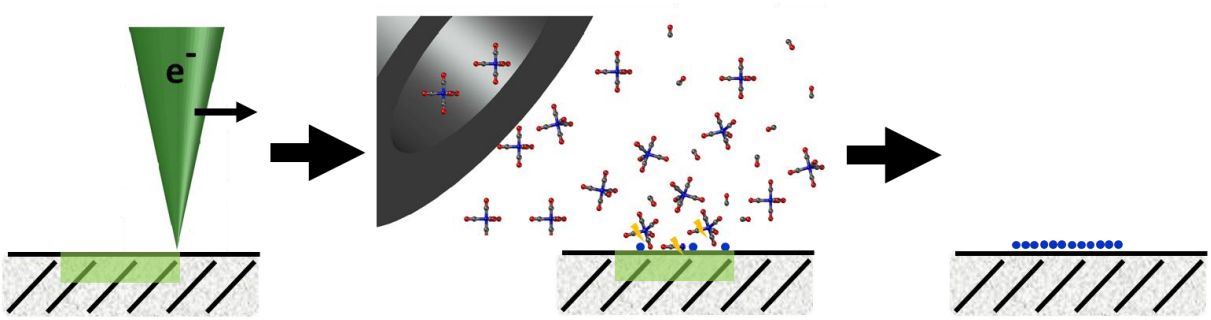

Figure 2-10: Scheme of the EBISA process. The surface is activated by the focused electron beam in absence of any precursor molecule. In a second step the precursor molecules are dosed via a nozzle and the pre-irradiated active areas cause the dissociation of the precursor molecules. A deposit is formed on top of the activated areas.

Directly compared to EBID, the EBISA process bears the advantage that the electron irradiation is separated from the precursor dosage and the growth of the deposit is controlled only via the precursor. Therefore, especially forward scattering proximity effects do not occur in EBISA at all. Consequently, EBISA is also a versatile technique to monitor BSE proximity effects and the electron scattering properties of different substrates without FSE.[9, 16, 128] Furthermore, in principle also the fabrication time can be reduced as deposits on pre-irradiated areas grow in parallel as long as the precursor is dosed.[7]

Of course, EBISA only works with a suitable combination of a substrate that can be activated and a precursor which reacts with the activated sites. The first successful EBISA experiment was conducted on a SiO_2(300nm)/Si surface with the precursor $Fe(CO)_5$ under UHV conditions.[8] With this precursor EBISA under UHV is also feasible on other surfaces like rutile TiO_2(110),[17] thin layer of porphyrin molecules[16-17] and surface-anchored metal-organic frameworks (SURMOFs).[15] A second precursor which shows successful EBISA results on a thin layer of porphyrin molecules under UHV is $Co(CO)_3NO$.[17] However, this precursor shows no reactivity towards the activated sites of SiO_2,[10] rutile TiO_2(110)[17] and SURMOFs.[15] UHV environment definitely seems to be beneficial for the EBISA process as the amount of residual gases which may react with the activated areas and thereby passivate them is reduced compared to high vacuum. Nevertheless, Muthukumar et al. showed that the precursor $Co_2(CO)_8$ leads to the formation of well-defined Co deposits on activated areas of SiO_2 by following the EBISA procedure in HV.[129]

For the oxide surfaces suitable for EBISA explored so far, the nature of the active sites caused by electron irradiation is well understood. Electron irradiation leads to a darkening of

the irradiated areas in SEM and further analysis of these areas by AES and scanning transmission microscopy (STM) reveals that ESD of oxygen yield oxygen vacancies in the substrate, which are identified as active sites for the initial decomposition of $Fe(CO)_5$.[8, 11, 14] The ESD of oxygen can be attributed to a Knotek-Feibelman process.[130-131] In the case of organic or metal-organic substrates it is known that electron irradiation of organic species can cause the cleavage of C-C or C-H bonds and hence induce the formation of reactive radicals and ions.[18, 69, 132] These radicals and ions might initiate the dissociation of the precursor molecules. However, the nature of the activated sites is still speculative especially due to the fact that on 2H-TPP EBISA is possible with $Fe(CO)_5$ and $Co(CO)_3NO$,[17] whereas on SURMOFs EBISA only works with $Fe(CO)_5$.[15] Therefore, the activation mechanism of organic and metal-organic substrates in EBISA seems to differ due to the complexity of the corresponding substrates. A relative simple organic substrate which is already well-studied regarding electron induced effects are SAMs.[18, 69, 132] In order to gain more insight into the underlying processes during electron irradiation a part of this thesis is devoted to electron induced effects and the reactivity towards EBISA of SAMs, porphyrins, and SURMOFs.

2.7.3 Autocatalytic Growth (AG)

Autocatalytic growth (AG) occurs when one of the reaction products catalyzes the reaction itself.[133] In EBID and EBISA this AG process occurs when the deposited material induces the dissociation of the precursor. The process for AG is depicted schematically in Figure 2-11. An initial deposit fabricated via EBID or EBISA can catalyze upon further precursor dosage the dissociation of the precursor. Thus, the deposit grows autocatalytically as long as the precursor is dosed. The precursors $Fe(CO)_5$ and $Co(CO)_3NO$ used in the thesis at hand both exhibit pronounced AG at room temperature (RT) under UHV conditions.

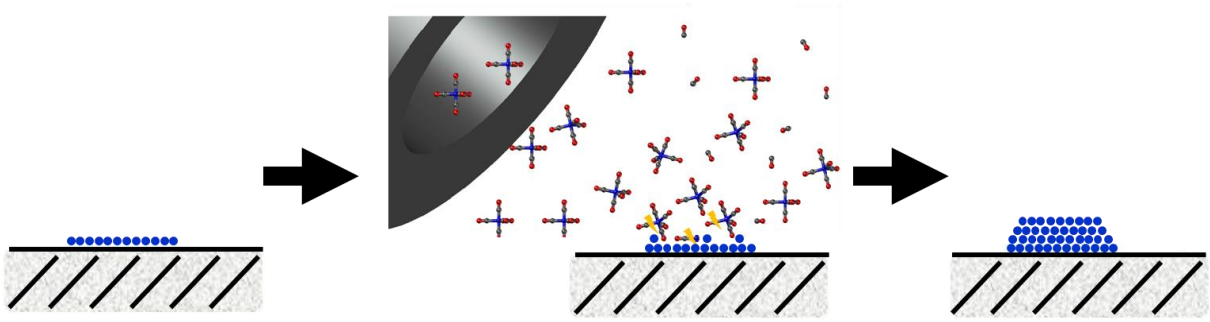

Figure 2-11: Scheme of the autocatalytic growth (AG) process. The initial deposit formed by EBID or EBISA is catalytically active towards the decomposition of the precursor molecule. Upon further precursor dosage the deposit grows.

AG behavior of $Fe(CO)_5$ at RT was reported on several substrates like Ag(111),[16] Pt(111)[134] and Rh(110).[135] The first insight about the AG of $Fe(CO)_5$ within an EBID experiment was given by Kunz et al. in 1987. They reported that at 125 °C thin layers of Fe fabricated via EBID induce the dissociation of the precursor and thus an AG process.[136-137] Under UHV conditions the AG on pre-deposited Fe nuclei, fabricated via EBID or EBISA, occurs already at RT.[8, 12] This AG process results in the formation of well-defined Fe deposits with high purity (≥ 95 at%).[12-15] The deposit consists mainly of α-Fe and a few amount of Fe_3O_4.[138] This remarkably high purity is only achievable by combining EBID or EBISA with the AG process. The nature and thus the purity of the final deposit is mainly determined by the AG process and not by the thin initial deposit fabricated via EBID or EBISA.

Vollnhals et al. studied the AG behavior of the precursor $Co(CO)_3NO$ by combining SEM, Scanning Transmission X-ray microscopy (STXM), and Near Edge X-ray Absorption Fine Structure Spectroscopy (NEXAFS) studies.[10] These studies revealed that the precursor $Co(CO)_3NO$ also grows autocatalytically. The resulting deposit shows a composition of $CoO_xN_yC_z$. In summary, the deposit consists mainly of cobalt oxide with small amounts of nitrogen and carbon. Remarkably, $Co(CO)_3NO$ decomposes autocatalytically on Fe seed layers.[10] Furthermore, the precursor $Fe(CO)_5$ also decomposes autocatalytically on the deposits fabricated with $Co(CO)_3NO$.[139] This opens up new methods for the fabrication of layered magnetic nanostructures without additional electron exposure.

Within this work, a combined EBID + AG respectively EBISA + AG approach was performed for the precursors $Fe(CO)_5$ and $Co(CO)_3NO$.

3 Results

Hybrid structures consisting of metallic nanostructures and organic respectively metal-organic substrates are versatile materials with huge application potential. One main goal of the thesis at hand is to explore novel methods to fabricate such structures and to systematically investigate the underlying processes. In this regard, three different types of organic/metal-organic substrates (SAMs, porphyrins, and SURMOFs) are functionalized with metallic nanostructures via FEBIP. Next to the fabrication of such hybrids, the thesis at hand focuses on the electron induced effects occurring on a molecular scale for the different substrates. Especially the underlying chemistry in the EBISA process on organic/metal-organic substrates, which is still not fully understood, is investigated in detail. Chapter 3.1 addresses a collaborative approach together with the group of Prof. Gölzhäuser from the University of Bielefeld and deals with SAMs and CNMs made from TPT. The Chapter consists of two parts. In the first part (Chapter 3.1.1), a new method for the fabrication of metallic iron nanostructures fabricated via EBID on top of 1 nm thick CNMs is introduced. The second part (Chapter 3.1.2) investigates this fabrication method in more detail especially regarding fundamental aspects of EBID and EBISA on SAMs and the effect of the substrate on the transfer process. Chapter 3.2 takes up the idea of transferable CNMs and expands the concept to a new class of molecules namely porphyrins (2H-TPP) which are in addition only physisorbed on the original substrate. The transfer mechanism introduced in Chapter 3.1.1 serves as evidence for the production of stable 2H-TPP membranes. Furthermore, in cooperation with the group of Prof. Swiderek, the electron induced effects of 2H-TPP were studied by ESD and RAIRS. The last part (Chapter 3.3) stems from the same cooperative effort and focuses on the underlying chemistry during EBISA on the SURMOF HKUST-1. Electron-induced effects on HKUST-1 and surface-grown copper(II)-oxalate, which only differ in the organic linker molecules, are compared by measuring AES, ESD, and RAIRS.

3.1 Exploring and modifying SAMs and CNMs via FEBIP [P1, P2]

Functional hybrid structures consisting of metallic nanostructures and non-metallic 2D materials are key components for novel applications in the field of electronics, optics and magnetics.[73-74, 140] In the following Chapter a new FEBIP-based approach for the fabrication of such functional hybrids is presented. The bottom-up grown SAM TPT is functionalized with top-down methods from FEBIP and subsequently transformed into a CNM. Thereby, different materials e.g., Au and Ag served as substrate for the growth of the SAM and were investigated within this fabrication process.

3.1.1 Fabrication of metallic nanostructures on 1 nm thick CNMs [P1]

A measure to fabricate novel hybrid nanomaterials was to combine the well-established method to fabricate CNMs via electron induced crosslinking of SAMs with our UHV approach to FEBIP. The goal was to fabricate laterally structured materials on top of an ultrathin membrane. In particular, it was investigated if the CNM remains intact with the FEBIP structure on top. To do so the method schematically depicted in Figure 3-1 was applied. A SAM consisting of TPT molecules on a Au(111)/mica sample was used as substrate. On this substrate EBID was performed with the precursor $Fe(CO)_5$ (cf. Figure 3-1a). Within the EBID process the irradiated areas of the SAM were presumably locally cross-linked, which is indicated by the red square. The sample with the ultraclean iron deposit (90 at%) on top was in a second step transformed into a CNM via large area electron irradiation via an electron flood gun (cf. Figure 3-1c). To protect the sample mechanically during the transfer, it was spin-coated with a 300 nm thick layer of poly(methyl methacrylate) (PMMA). Subsequent etching of the Au layer in a solution of $KI/I_2/H_2O$ within 10 minutes enabled the lift-off from the mica substrate (cf. Figure 3-1d). During this step, the iron structure was protected as it was sandwiched in between the PMMA and the CNM. This sandwich structure was then transferred onto either SiO_2 (cf. Figure 3-1f) or transmission electron microscopy (TEM) grids (cf. Figure 3-1e) in the latter case to obtain free-standing CNMs with metallic nanostructure on top. In a last step, the PMMA layer was removed by dissolution in acetone. The real dimensions of the resulting hybrid structures are depicted in Figure 3-1g. The CNM with a thickness of ~1.2 nm needs to hold a metallic

nanostructure with roughly 15 nm height during the whole transfer. A critical point to investigate was if the CNM is mechanically stable enough for such a transfer. Furthermore, the iron structures were analyzed in detail before and after the transfer to evaluate changes which might occur during the transfer process.

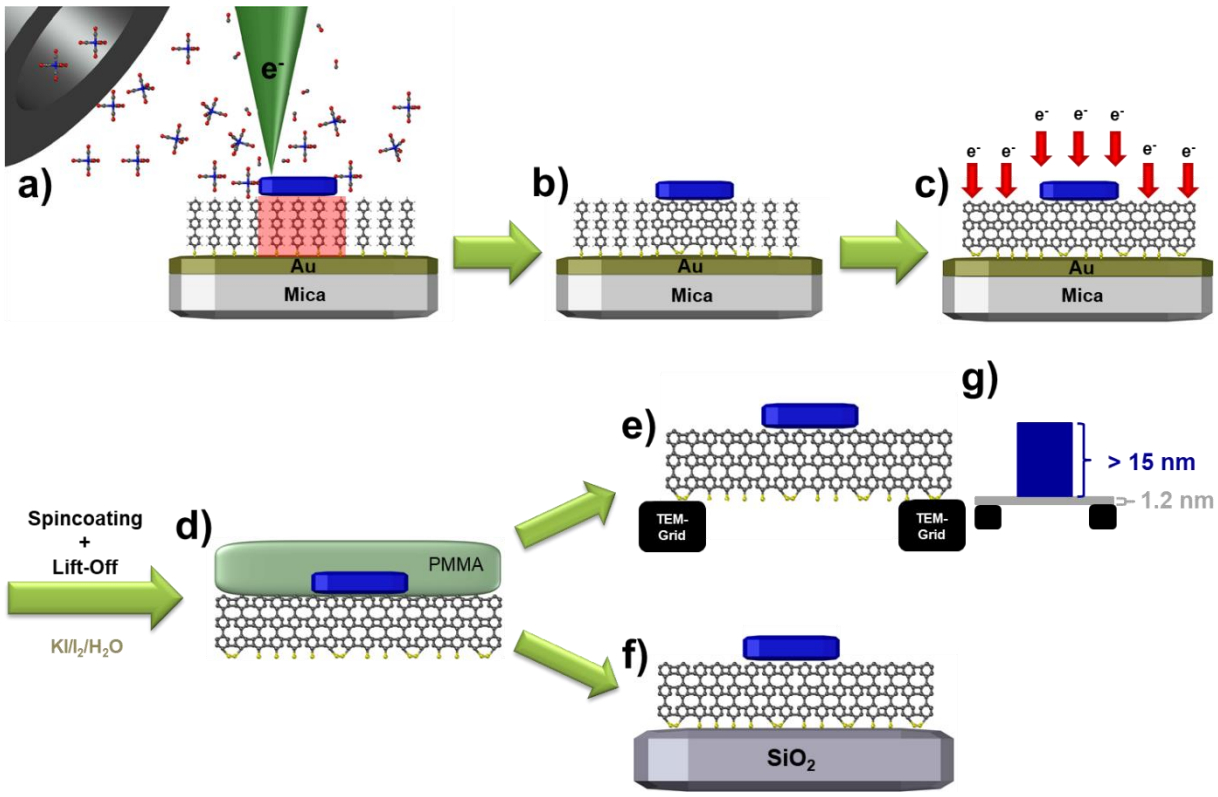

Figure 3-1: Scheme of the fabrication process: a) EBID of $Fe(CO)_5$ onto a TPT SAM on Au/mica; the blue feature is the resulting Fe EBID deposit; the red square indicates that during EBID simultaneously the irradiated area of the SAM is crosslinked; b) Fe nanostructure on TPT SAM; the area below the nanostructure is already transformed into a CNM; c) cross-linking of aromatic SAM with low energy electrons (≈50 eV) via flood gun; d) sample is spin-coated with PMMA and removed from the substrate by etching the Au layer with $KI/I_2/H_2O$; e,f) membrane is transferred onto TEM grid or onto SiO_2, PMMA is removed by acetone; g) real dimensions of a typical aerial Fe deposit on top of a CNM. Adapted from [P1].

In Figure 3-2 the results of the transfer process are depicted. The SEM images of two different iron nanostructures with the shape of a CNM fabricated via EBID are shown in Figure 3-2a and b. One of these structures was transferred onto a SiO_2 sample (cf. Figure 3-2d) and the other one onto a TEM grid (cf. Figure 3-2c). Both structures remained intact after the transfer process. The small ruptures in the CNM (see red circles in Figure 3-2c) were most probably caused by the particles located on the sample already before the transfer (see red circles in Figure

3-2a). The width of the structures is in the range of 60 to 75 nm. The height was measured by AFM and was between 2 and 4 nm. These results prove that the fabrication process works and complex hybrid structures e.g., iron nanostructures on top of a freestanding 1.2 nm thin organic membrane can indeed be fabricated with this approach.

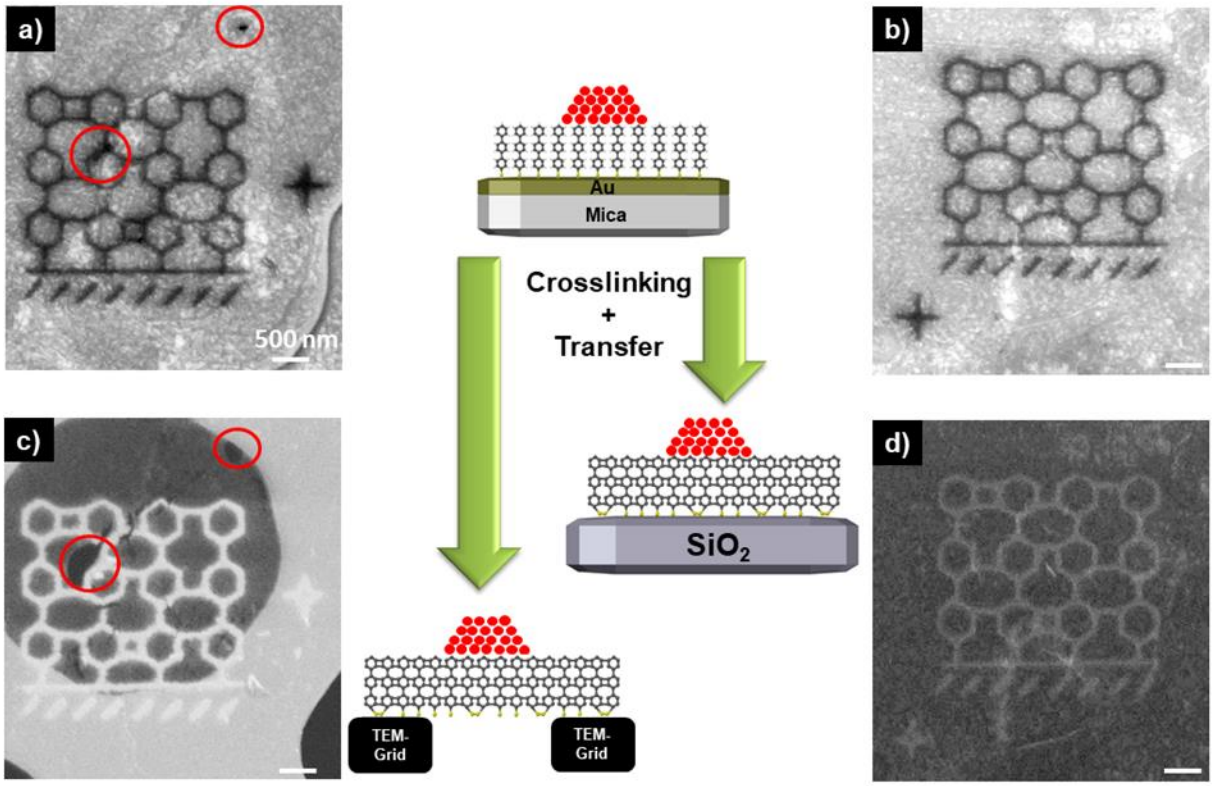

Figure 3-2: Schematic drawing of the transfer process and the corresponding SEM images of a) EBID nanostructure on TPT on Au(111)/mica fabricated with the precursor $Fe(CO)_5$ (beam parameters: 15 kV, 400 pA, electron dose: 1.86 C cm^{-2}, AG time: 1 h); b) EBID nanostructure on TPT on Au(111)/mica fabricated with the precursor $Fe(CO)_5$ (beam parameters: 15 kV, 400 pA, electron dose: 2.07 C cm^{-2}, AG time: 1 h 27 min); c) the nanostructure depicted in (a) after transfer onto TEM grid; the red circles indicate positions of particles/defects before the transfer, which obviously lead to ruptures in the freestanding CNM; d) the nanostructure depicted in (b) after transfer process onto SiO_2. Adapted in part from [P1].

In order to analyze the chemical composition of the transferred iron structures a larger iron marker structure was fabricated via EBID on a SAM of TPT on Au(111)/mica (cf. Figure 3-3a). The SAM was cross-linked and transferred together with the iron marker structure onto a solid SiO_2 substrate. Even for the larger structure, which is approximately 10 to 20 times thicker than the actual membrane no obvious changes in size and shape were visible after the transfer

(cf. Figure 3-3b). In the corresponding blow-up image, the characteristic iron nanocrystals which are formed during AG[8, 14, 39] were still visible after the transfer (cf. Figure 3-3c). AES spectra reveal that the structure was oxidized during the transfer process (cf. Figure 3-3d). However, this chemical change was to be expected as the transfer partially occurred under ambient conditions. In addition, a rather high amount of carbon was detected on the structure directly after transfer. This carbon contamination was probably caused by residual PMMA and it was verified by subsequent AES that this impurity can easily be removed with 5 minutes of argon sputtering. After removing the residual PMMA the iron oxide structure contained an Fe content of 84 at% which is comparable to literature values of oxidized iron structures.[13-14] The latter results evidence that the shape of the nanostructures is not influenced by the transfer process. The chemical composition was beside from oxidation not strongly affected.

Regarding the huge amount of available precursors for FEBIP[4] and its high potential for the direct fabrication of nanostructures with arbitrary shape and size,[3-5, 98] this new fabrication process opens up the possibility to produce complex hybrid structures with high potential for applications in nanoelectromechanical systems (NEMS) or photonic devices.

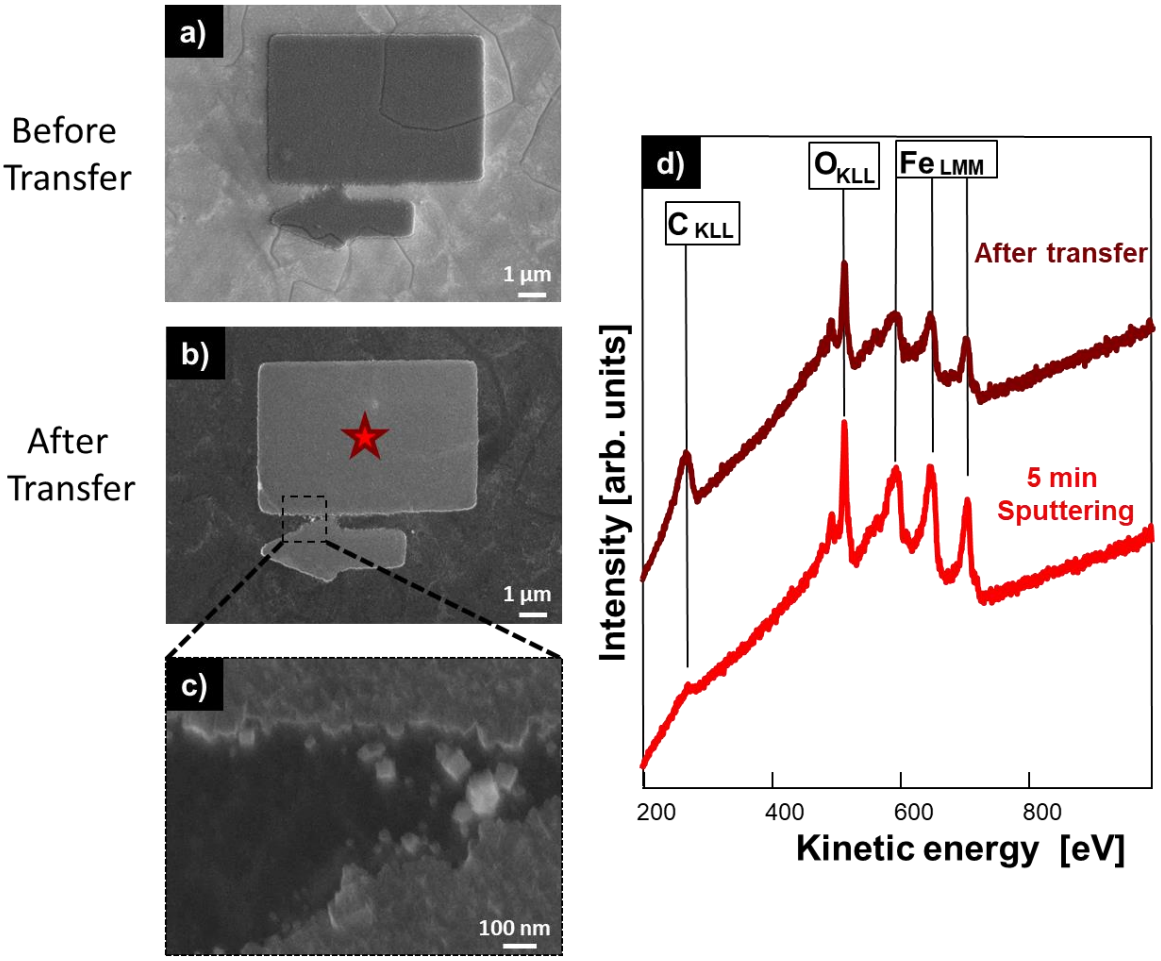

Figure 3-3: a) SEM image of a large Fe marker structure fabricated with EBID on SAM TPT on Au(111)/mica (beam parameters: 15 kV, 400 pA, electron dose: 0.93 C cm^{-2}, AG time: 8 h 46 min); b) SEM image of the large Fe marker structure depicted in (a) after the transfer to bulk SiO_2; c) SEM zoom-in of detail in (b); d) local AE spectra recorded at the position indicated with the colored star. Adapted in part from [P1].

3.1.2 Detailed investigation of FEBIP and the transfer mechanism on TPT on Ag[P2]

The proof of concept of the new fabrication method for complex hybrid materials was presented in the previous Chapter with a SAM of TPT on a Au(111)/mica substrate. For a better fundamental understanding, a detailed investigation of the underlying processes yielding such hybrid nanostructures was performed. Thereby, the fabrication and transfer method was explored on a SAM of TPT grown on a Ag(111)/mica substrate, i.e. the substrate was changed from Au to Ag. It is important to study the effect of the underlying substrate and the associated effect on the resulting transferred hybrid structures, as for example carboxylic anchor group-based SAMs can be fabricated on Ag.[141-142] The change of substrate comes along with a change in the wet-chemical transfer process which will be discussed later. First, the results for the EBID and EBISA experiments with the precursors $Fe(CO)_5$ and $Co(CO)_3NO$ are briefly discussed.

EBID was successfully conducted with both precursors on a SAM of TPT on Ag(111)/mica. For the iron deposits (92 at% Fe) as well as the cobalt oxide deposits (45 at% Co, 45 at% O, < 10 at% C and N) purities comparable with previous literature values were achieved.[10, 14-15, 17, 135] However, EBISA was only driven successfully with the precursor $Fe(CO)_5$. A well-defined iron deposit with a purity of roughly 90 at% Fe and the characteristic iron nanocrystals was fabricated. The $Co(CO)_3NO$ precursor did not react with the active surface sites and therefore no cobalt oxide deposit was formed. The SAM exhibits a chemical selectivity between the two precursors in the EBISA process, similar to other substrates e.g., HKUST-1,[15] SiO_2[10]. Surprisingly thin layers of 2H-TPP molecules do not show such a selectivity and EBISA was conducted successfully with both precursors.[17] Further investigations on a bare Ag(111)/mica substrate proofed that the SAM itself is the active substrate during the EBISA process. In addition, it could be demonstrated that as soon as the whole SAM is cross-linked into a CNM by low energetic electron irradiation, EBISA with $Fe(CO)_5$ did not work anymore. It is known that during electron irradiation the C-H bonds of the TPT molecules are cleaved by dissociative electron attachment and new C-C bonds are formed between neighboring TPT molecules.[69] The free radicals formed after the cleavage of the C-H bond might be the active species causing the reaction with $Fe(CO)_5$. In the framework of the thesis at hand, it was indeed possible for the first time to further investigate the lifetime of the active species. Interestingly it

turned out that the lifetimes of the active species, i.e., presumably the mentioned free radicals/activated C atoms, ranged to hours.

Thus, the lifetime of the activated sites in EBISA was analyzed in detail by studying the waiting time between electron irradiation (3 nA, 15 kV) and precursor gas dosage. Three different electron doses (1.01 C cm^{-2}, 3.12 C cm^{-2}, 6.08 C cm^{-2}) were investigated with regard to four different waiting times (5 min, 92 min, 140 min, 155 min). The results for this experiment are depicted in Figure 3-4. At short waiting times the whole irradiated areas (2 x 2 μm^2 squares) for all three doses were covered with clean (cf. AE spectra) iron deposits. However, for longer waiting times the iron deposits appeared reduced in size step by step and the deposit areas appeared more and more depleted. The lower the electron dose, the faster this process occurred. Therefore, one could conclude that the EBISA process on the SAM-TPT shows a strong time dependence, i.e., the activated sites exhibit a certain lifetime. This is rather surprising as such a time dependence was not reported before to my best knowledge. As an example on SiO_2 the active areas still react with $Fe(CO)_5$ after two days of waiting time.[8]

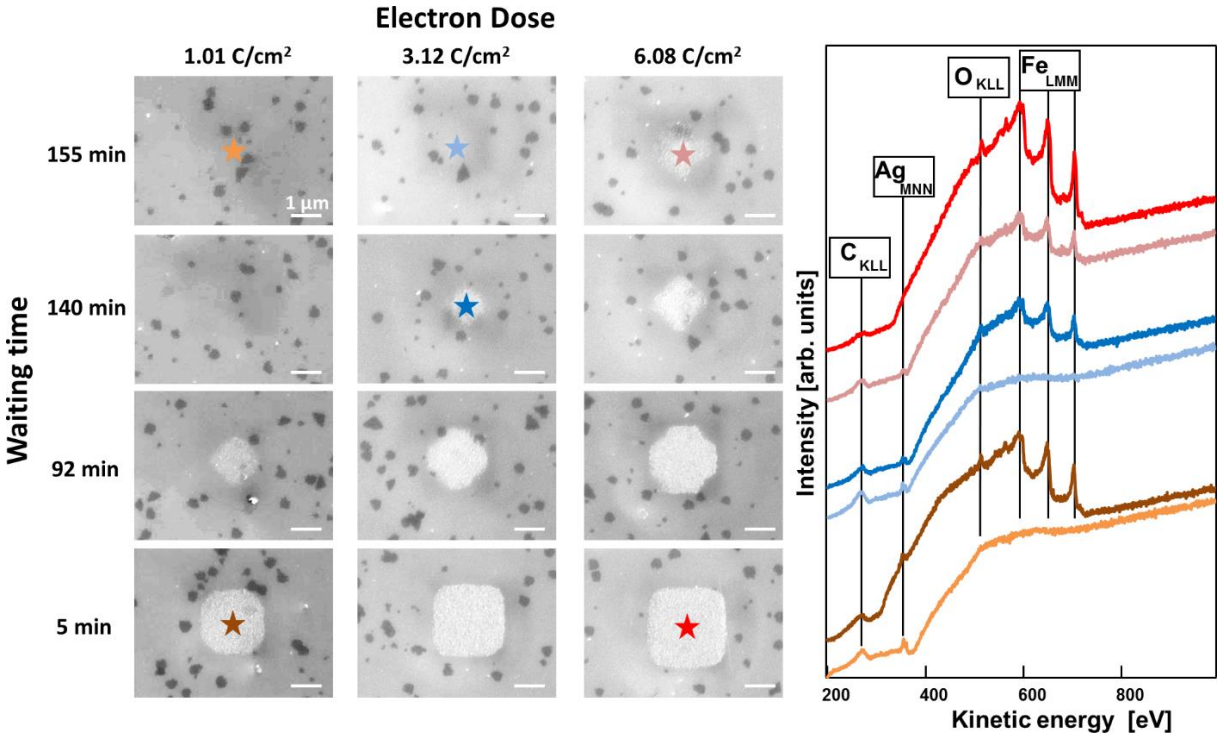

Figure 3-4: Results of time dependent EBISA experiments followed by autocatalytic growth on TPT SAM on Ag(111)/mica. All structures were written with E_{beam} = 15 kV, I_{beam} = 3 nA and exhibit the same t_{AG} = 3 h 29 min; The SEM images of a 2 x 2 µm² deposit fabricated via EBISA + AG with $Fe(CO)_5$ can be differentiated regarding electron dose (left column: 1.01 C cm^{-2}; medium column: 3.12 C cm^{-2}; right column: 6.08 C cm^{-2}) and waiting time between electron irradiation and precursor dosage. Local AE spectra recorded at the positions indicated with respectively colored stars. Adopted from [P2].

One possibility for this time deactivation could be the previous explained mechanism for the formation of C-C bonds out of cleaved C-H bonds. In this picture, the time interval until all radicals from cleaved C-H bonds form new C-C bonds equals the lifetime of the active sites in the EBISA process. However, it could also be possible that the reactive radicals were either deactivated by reactions with residual gases in the UHV chamber or an electron quenching effect via the surface or neighboring molecules.[69] These results demonstrate that there are still ambiguities within the EBISA process on organic substrates and there is a strong scientific demand to further study this process. Chapter 3.3 will strongly focus on the underlying chemistry during the EBISA process by investigating electron induce processes in the SURMOF HKUST-1 in detail.

The transfer mechanism shown in Figure 3-1 worked out with a SAM of TPT grown on a Au(111)/mica substrate. In this study, the complex fabrication and transfer mechanism is expanded to a SAM of TPT grown on a Ag(111)/mica substrate. The transfer scheme was as

described in Chapter 3.1.1, except the wet-chemical lift-off process differed. The sample was placed in a solution of $Fe(NO_3)_3$ for 24 h in order to dissolve the Ag and perform the lift-off. In the following, the effects of this change on the process are summarized. In Figure 3-5 the results for the transfer of a CNM, with an iron marker structure fabricated via EBID, onto SiO_2 are depicted. Before the transfer, the well-defined marker structure consists of the characteristic iron nanocrystals formed during AG (cf. Figure 3-5a and b). Local AE spectrum revealed that the deposit had a purity of 87 at% iron (cf. Figure 3-5e). After the transfer, a bright circular shape was located around the structure (cf. Figure 3-5c). Furthermore, no iron nanocrystals were visible in the corresponding blow-up image anymore (cf. Figure 3-5d). The structure was oxidized during the transfer process and also the bright circular feature in the surrounding consists of iron oxide (cf. Figure 3-5e). AFM images before and after the transfer process evidenced that the iron structures are decreasing in height during the transfer. Apparently the $Fe(NO_3)_3$ solution caused significant changes on the iron structure. It is assumed that the $Fe(NO_3)_3$ solution diffused through the PMMA/CNM and causes a dissolution/reduction of the iron structures. Such a dissolution process might also explain the bright circular feature around the iron structure.

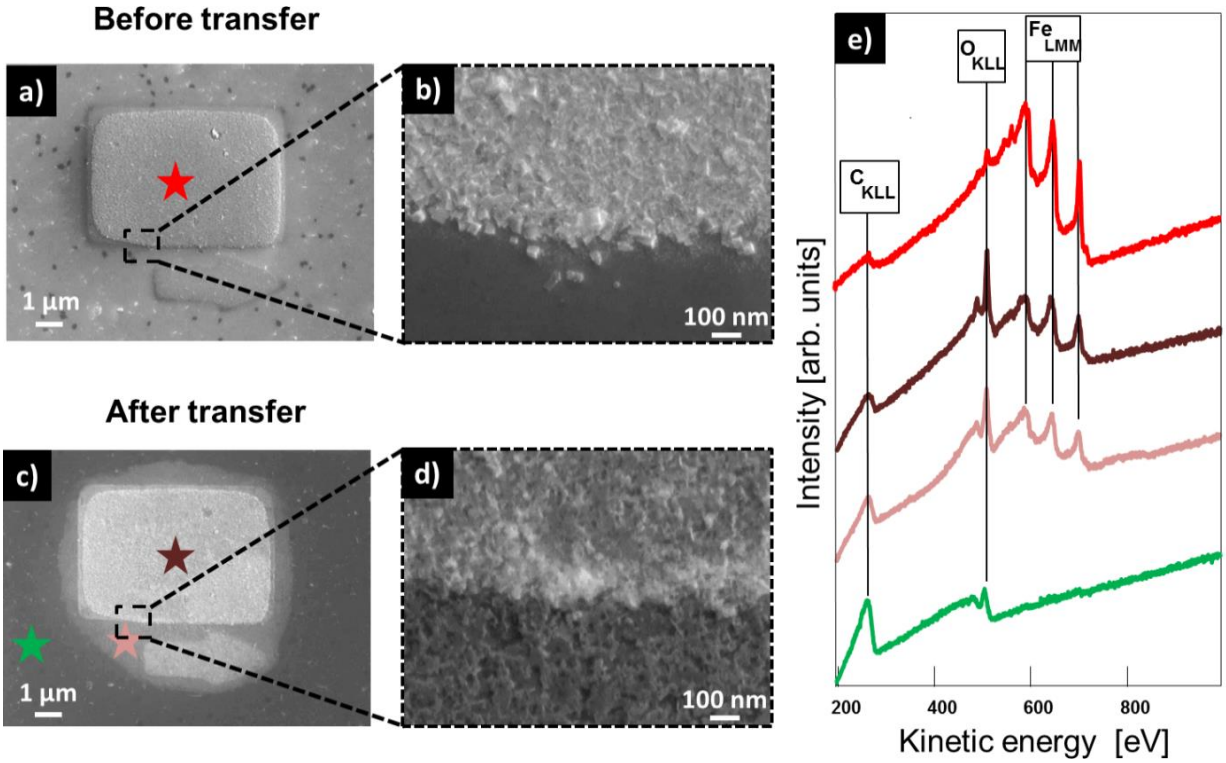

Figure 3-5: Transfer of a CNM with Fe structure on top onto a SiO_2 sample. a) SEM image of a Fe structure fabricated with EBID on TPT SAM on Ag(111)/mica (beam parameters 15 kV, 400 pA, electron dose: 0.93 C cm^{-2}, AG time: 4 h 5 min) b) Blow-up image of the structure depicted in a); c) SEM image of the Fe structure depicted in a) after the transfer to bulk SiO_2; d) Blow-up image of the structure depicted in c); e) local AES spectra recorded at the positions indicated with respectively colored stars. Adopted from [P2]

The same transfer process was also performed with a structure fabricated from $Co(CO)_3NO$ with EBID + AG. In this system the $Fe(NO_3)_3$ solution also caused problems during the transfer process. The well-defined cobalt oxide structure located on the SAM/CNM before the transfer is completely gone after the transfer process. This was proven by SEM, AES, and AFM. Apparently the $Fe(NO_3)_3$ solution caused the complete dissolution of the cobalt oxide structure.

Consequently, the system SAM on Ag(111)/mica combined with a $Fe(NO_3)_3$ solution for the lift-off is not a suitable system for the fabrication of hybrid structures containing iron or cobalt oxide nanostructure. However, it might be a suitable system for hybrids containing more inert nanostructures like gold or platinum. These results underline the need to study the effects of the underlying substrate and the corresponding chemistry to dissolve the latter in such type of transfer processes.

3.2 Ultrathin CNMs from 2H-TPP [P3]

In this Chapter the field of 2D organic membranes is expanded from CNMs fabricated from wet-chemically prepared SAMs to CNMs fabricated from physisorbed molecular layers of 2H-TPP molecules prepared by physical vapor deposition in UHV. This is an important finding, since it also considerably expands the possibilities to prepare the organic substrates, i.e., away from a lengthy wet-chemical procedure as in the case of SAMs to an *in situ* preparation of the molecular layer in the vacuum chamber. Furthermore, the outstanding properties of porphyrins in nature and technology make them interesting candidates for the formation of CNMs. Previous studies also demonstrated the possibility to perform EBID and EBISA with $Fe(CO)_5$ and $Co(CO)_3NO$ and strongly reduced proximity effects on thin layers of 2H-TPP.[16-17] The transfer mechanism introduced in Chapter 3.1.1 was used to show the feasibility to create stable CNMs out of 2H-TPP with metallic nanostructures on top.

First, the processes occurring on a molecular scale during electron irradiation of thin layers of 2H-TPP are discussed. The RAIRS and ESD experiments were performed at the University of Bremen in a cooperative effort with the group of Prof. Petra Swiderek. ESD measurements on thin layers of 2H-TPP showed that during electron irradiation (electron energy of 100 eV) besides from hydrogen no further fragments desorbed from the surface. The hydrogen formation is caused by the electron induced cleavage of C-H bonds which also occurs during electron irradiation of SAMs.[18, 69, 143-144] The 2H-TPP sample was analyzed by RAIRS before and after electron irradiation. Before electron irradiation the typical vibrational modes at 801 cm^{-1} (out-of-plane deformation porphyrin ring), 966 cm^{-1} (porphyrin ring vibration), 702 cm^{-1} (out-of-plane deformation of the phenyl substituent), 732 cm^{-1} (out-of-plane bending vibration N-H bond), 3317 cm^{-1} (N−H stretching vibration), 1469 cm^{-1} (CC stretching vibrations porphyrin ring) and 1596 cm^{-1} (CC stretching vibrations phenyl substituent) could be assigned. The sample was irradiated with low energetic electrons (100 eV) until no hydrogen development was observed anymore in QMS (173 C cm^{-2}). After electron irradiation almost all characteristic vibrational bands of 2H-TPP have vanished, except some small contributions from the vibrational modes at 1469, 702, and 801 cm^{-1}. Furthermore, a broadening of the bands in the region of 1596 cm^{-1} was observed. Therefore, it was concluded that the C-H as well as the N-H bonds of the 2H-TPP molecules are cleaved upon electron irradiation and that the resulting

reactive radicals might react with neighboring 2H-TPP molecules to form a cross-linked 2H-TPP membrane.

The transfer process shown in Figure 3-1 was used to prove the formation of a stable CNM fabricated by electron induced cross-linking of thin layers of 2H-TPP molecules. Therefore, a 1.5 nm thick layer of 2H-TPP molecules was evaporated onto a clean Au(111)/mica substrate. EBID and EBISA was performed onto that sample and afterwards the same transfer protocol as described in Chapter 3.1.1 for SAMs was executed. The results for the transfer onto a TEM grid are depicted in Figure 3-6. Figure 3-6a depicts a SEM image of a 2 x 2 μm^2 square fabricated via EBISA + AG with the precursor $Fe(CO)_5$. The corresponding blow-up image (cf. Figure 3-6b) reveals the characteristic iron nanocrystals and local AES (cf. Figure 3-6c) confirmed the high purity of the deposit. It mainly consists of iron with small impurities of carbon and oxygen. In Figure 3-6d the same structure is depicted after the sample was transferred onto a TEM grid. The deposit is located where no support from the TEM grid is available and therefore it is only held by the 1.5 nm thick cross-linked 2H-TPP CNM (cf. green circle in Figure 3-6d). This experiment proofs the formation of stable CNMs via electron induced cross-linking of 2H-TPP molecules. There are some ruptures within the membrane visible (cf. red areas in Figure 3-6d), however these were probably caused by electron irradiation during image acquisition. Local AES (cf. Figure 3-6c) and the corresponding blow-up image (cf. Figure 3-6e) show that the structure is beside from oxidation not changing in size, shape and chemistry.

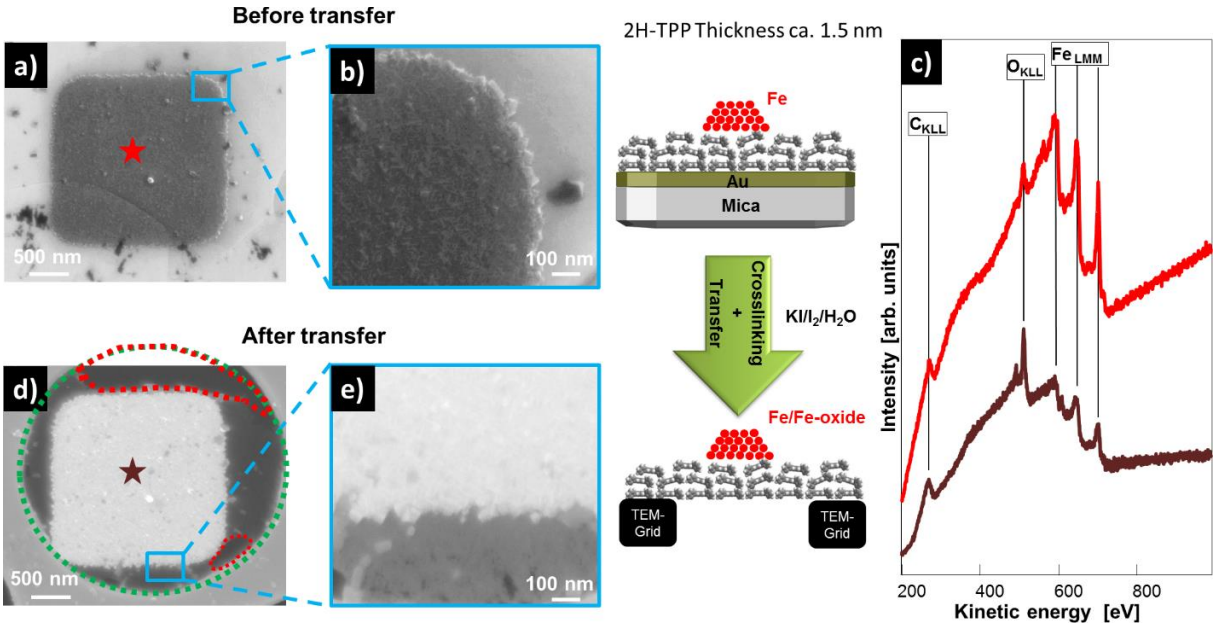

Figure 3-6: Transfer of a 2H-TPP CNM with Fe structure on top onto a TEM grid. a) SEM image of a Fe structure fabricated with EBISA on 2HTPP on Au(111)/mica (beam parameters: 15 kV, 3 nA; electron dose: 6.24 C cm^{-2}; AG time: 4 h 46 min). b) Blow-up image of the structure depicted in (a). c) Local AES spectra recorded at the positions indicated with colored stars. d) SEM image of the Fe structure depicted in (a) after the transfer onto a TEM grid. The green circular shape marks the area where the membrane is completely free-standing while the areas marked by the red dotted line indicate the rupture of the membrane. e) Blow-up image of the structure depicted in (d). Adopted from [P3].

Next to this, a 2H-TPP sample with a structure fabricated via EBID + AG with the precursor $Fe(CO)_5$ was cross-linked and transferred onto a solid SiO_2 substrate. Again, beside from oxidation the structure did not change during the transfer. This study demonstrates for the first time that it is possible to fabricate stable CNMs by low energetic electron crosslinking of physisorbed 2H-TPP molecules.

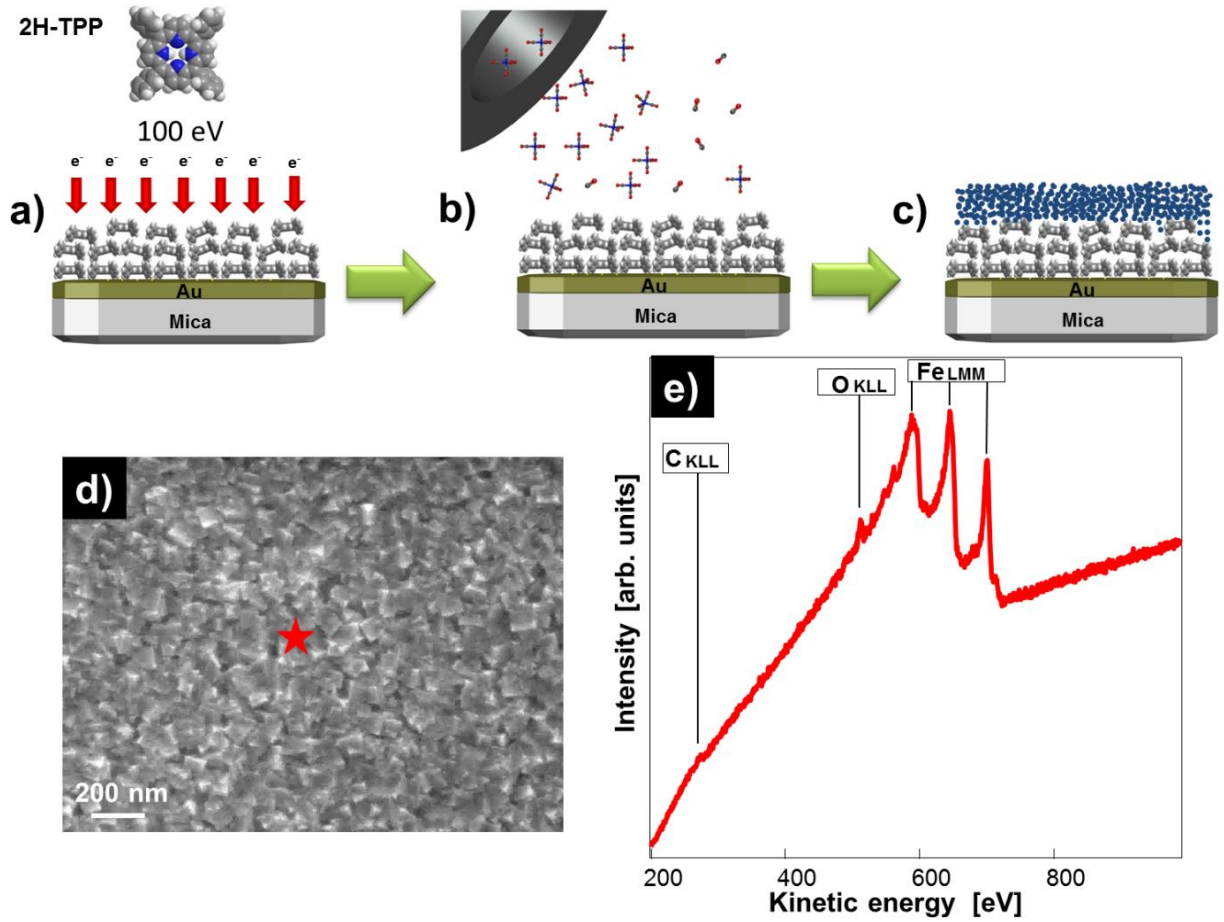

Figure 3-7: EBISA-like process with low-energy electrons. a) Irradiation of thin layers of 2H-TPP molecules with low-energy electrons (100 eV; 120 mC cm^{-2}) by a flood gun. b) Dosage of the $Fe(CO)_5$ precursor for 4 h. c) Cross-linked 2H-TPP CNM with Fe nanocrystals on top. d) SEM image of the cross-linked 2H-TPP CNM with Fe nanocrystals on top. e) Local AES spectra recorded at the position indicated with the colored star. Adopted from [P3].

Another interesting result that was investigated during these experiments is schematically depicted in Figure 3-7. Figure 3-7 shows a "large-area" EBISA approach. Instead of the focused electron beam an electron flood gun (electron energy 100 eV) was used to activate the 2H-TPP molecules on a macroscopic scale. After the dosage of $Fe(CO)_5$ for 4 h the whole surface was covered with ultra-clean iron nanocrystals as the SEM image (cf. Figure 3-7d) and the local AES spectra (cf. Figure 3-7e) evidence. By following this approach versatile layered 2D hybrid structures could be fabricated. Furthermore, this process shows that in EBISA already electrons with rather low energy are sufficient for the formation of the active species. In general, this result indicates that low energetic electrons are more effective in surface activation.

In this study it was shown that porphyrins, which are of high scientific interest and play a crucial role in nature, can be used for the fabrication of stable 2D materials. This opens up a

novel pathway for the tailored functionalization of the latter. The analyzed transfer process proofs the flexibility and high mechanical stability of the 2H-TPP CNMs. Furthermore, the electron induced mechanisms occurring on a molecular scale were analyzed.

3.3 Unraveling electron-induced effects on HKUST-1 during EBISA [P4]

A recent study by Drost et al. showed that SURMOFs e.g., HKUST-1 are a suitable substrates in FEBIP for the fabrication of spatially well-defined sub-10 nm structures.[15] Interestingly, the EBISA process exhibits the same chemical selectivity between the two precursors $Fe(CO)_5$ and $Co(CO)_3NO$ on HKUST-1 as on the SAM of TPT molecules (Chapter 3.1.2): EBISA was driven successful with $Fe(CO)_5$, however $Co(CO)_3NO$ showed no reactivity towards the activated sites.[15] The underlying chemistry during the EBISA process was not yet analyzed and is still speculative. Therefore, in this Chapter a detailed investigation of the EBISA process on the SURMOF HKUST-1 is presented. Thereby, HKUST-1 and a sample of surface-grown copper(II)-oxalate were investigated in terms of EBID & EBISA with both precursors. The main difference between the two substrates is the organic linker molecule (cf. Figure 2-6). The surface-grown copper(II)-oxalate lacks the aromatic ring in the organic linker. Furthermore, AES, RAIRS, and ESD were conducted to identify the chemical species that trigger the decomposition of the precursor molecules. The HKUST-1 sample and the surface-grown copper(II)-oxalate substrate were fabricated by the group of Prof. Swiderek from the University of Bremen.

The HKUST-1 sample in this approach was prepared via the conventional dipping method with a thickness of 65 nm. Drost et al. used a sample prepared by a spray method with an overall thickness of 150 nm.[15] Therefore, it was first analyzed whether the different preparation methods lead to the same qualitative result in EBID and EBISA. It could be demonstrated that the qualitative outcome was the same as already reported: EBID was successfully conducted with both precursors. However, EBISA works for $Fe(CO)_5$ but not for $Co(CO)_3NO$.

The electron induced effects on HKUST-1 and copper(II)-oxalate were studied by AES. The results are depicted in Figure 3-8. The grey spectra in Figure 3-8a and b represent the pristine HKUST-1 respectively copper(II)oxalate sample, whereas the black spectra were recorded after electron irradiation with a dose of roughly 9 C cm^{-2}. In Figure 3-8c and d the normalized peak areas are plotted for several electron doses. For both substrates the oxygen peak was drastically decreasing with increasing electron dose. With increasing electron dose, the C_{KLL} and the Cu_{KLL} peaks were remaining more or less constant for HKUST-1. This is in

good agreement with literature as it was reported that electron irradiation of HKUST-1 leads to the formation of copper nanoparticles embedded into a carbonaceous matrix.[145] In the case of copper(II)-oxalate the Cu_{LMM} peak was increasing with increasing electron dose. Again this is confirmed by literature as for copper(II)-oxalate clean copper nanoparticles without carbonaceous matrix can be fabricated via electron irradiation.[146] The remaining carbon can be attributed to the underlying SAM.

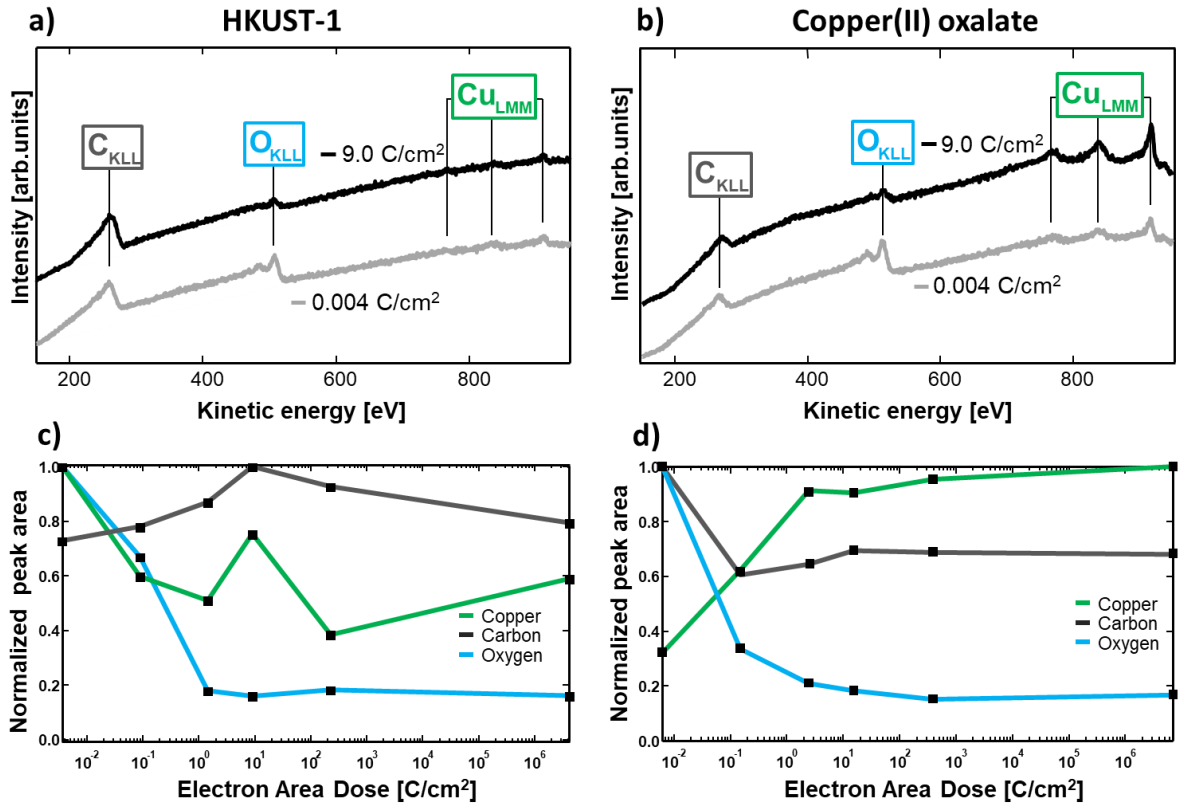

Figure 3-8: a, b) AE spectra recorded on HKUST-1 and copper(II)-oxalate samples, while scanning the surface with different SEM magnifications, and therefore different electron exposures with E_{beam} = 15 keV and I_{beam} = 3 nA. The gray curve is comparable to the pristine material, while the dose applied for the black curve is in the range of the EBISA process. c, d) Plot of the peak areas (after a linear background subtraction), each normalized to the most intense signal for a given element, against the electron area dose for HKUST-1 and copper(II) oxalate samples. Adopted from [P4].

The results for the EBID and EBISA experiments on the surface-grown copper(II)-oxalate are depicted in Figure 3-9. Figure 3-9a and Figure 3-9b each depict a SEM image of a 4 x 4 µm² square fabricated via EBID + AG with the precursor $Fe(CO)_5$ respectively $Co(CO)_3NO$. In both cases a well-defined deposit is visible. AES revealed that the iron deposit mainly consisted of pure iron with minor amounts of carbon and oxygen, whether the deposit fabricated from

$Co(CO)_3NO$ was composed of cobalt oxide with minor amounts of carbon and nitrogen (cf. Figure 3-9d). The results for the EBISA process with $Fe(CO)_5$ on copper(II)-oxalate are depicted in Figure 3-9c. Here, no clear deposit is visible, instead only a faint contrast is visible in the SEM image. Local AES proofed that no iron was deposited as only the characteristic auger peaks of the cooper(II)-oxalate were detected. Next to this, EBISA was also not successful with $Co(CO)_3NO$ on the copper(II)-oxalate substrate. These results indicate that the aromatic ring in the organic linker molecule of the HKUST-1 plays a crucial role in the activation process during EBISA with $Fe(CO)_5$. Furthermore, the copper nanoparticles can be ruled out as active sites during the EBISA process.

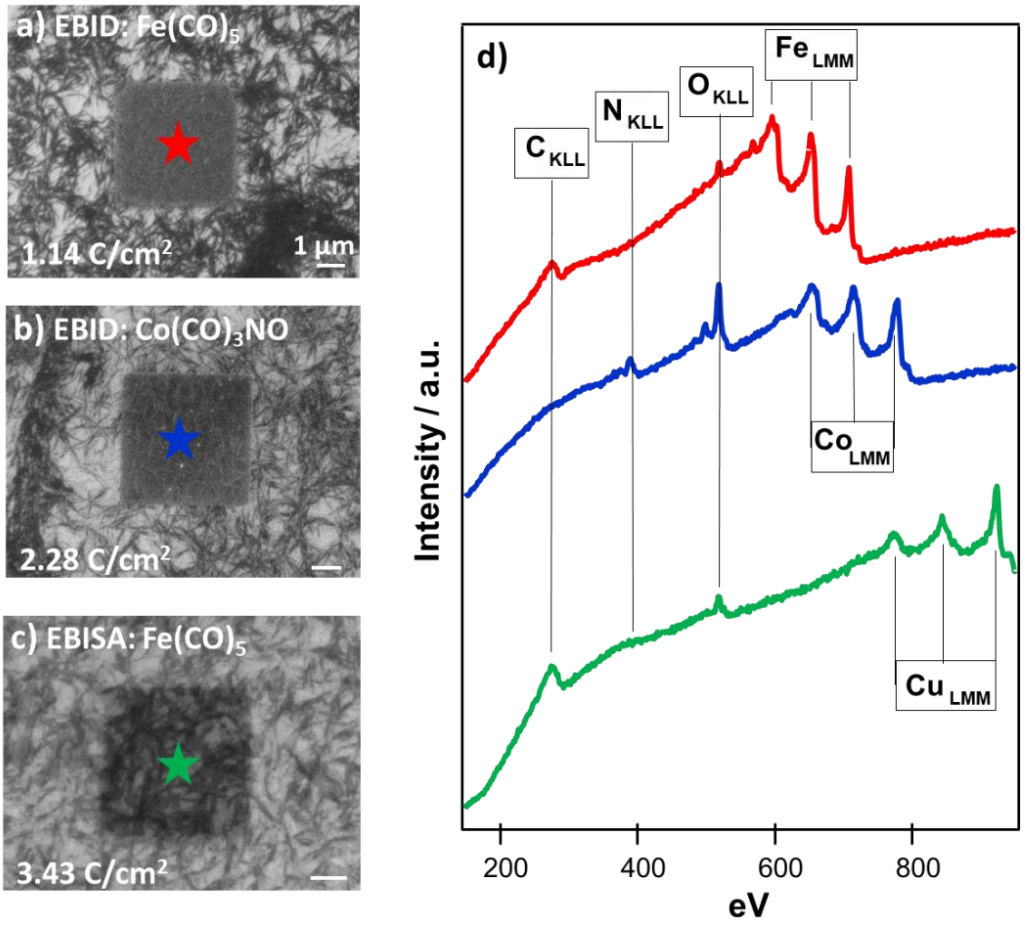

Figure 3-9: Results of FEBIP experiments followed by AG on copper(II)-oxalate. All structures were written with E_{beam} = 5 keV, I_{beam} = 400 pA. a) SEM images of a 4 × 4 µm² EBID + AG deposit fabricated from $Fe(CO)_5$ (1.14 C cm^{-2} and t_{AG} = 3 h 45 min), b) SEM image of a 4 × 4 µm² EBID + AG deposit fabricated from $Co(CO)_3NO$ (2.28 C cm^{-2} and t_{AG} = 4 h 4 min), c) SEM image of an EBISA + AG experiment with $Fe(CO)_5$ (3.43 C cm^{-2} and t_{AG} = 4 h 30 min) where no clear deposit can be observed from the SEM image contrast (the same result was obtained for the EBISA + AG experiment with $Co(CO)_3NO$), and e) local AE spectra recorded at the sites indicated with the respectively colored stars. Adopted from [P4].

To gain further inside into the chemical processes occurring during EBISA the effects of electron irradiation were studied via RAIRS and ESD. For copper(II)-oxalate RAIRS and ESD showed that the organic linker was completely decomposed under the formation of CO_2 upon electron irradiation. RAIRS of the HKUST-1 sample indicated that the organic linker molecule was only partly decomposed. The most significant changes were observed for the carboxylate stretching bands. This finding correlated well with the ESD results in which solely CO_2 was detected and no other fragments from the organic linker. Several different electron induced chemical reactions known from literature were discussed for HKUST-1. The different possible reaction products were analyzed with regard to their ability to cause the decomposition of $Fe(CO)_5$. However, from the fact that the copper nanoparticles are not the active site in the EBISA process, the actual activation mechanism could not be fully identified. Therefore, further studies regarding EBISA and electron induced reactions on different organic substrates need to be performed to gain deeper understanding in the underlying chemistry.

4 Summary

In the thesis at hand functional hybrid structures consisting of metallic nanostructures produced via FEBIP on top of organic or metal-organic substrates were fabricated and analyzed. Furthermore, a detailed investigation of the electron induced chemistry, especially during the EBISA process, was presented for three different substrates. The substrates analyzed within this thesis are SAMs respectively CNMs consisting of TPT molecules, thin layers of 2H-TPP molecules and the SURMOF HKUST-1. The FEBIP experiments were performed at room temperature in an UHV chamber. The morphology of the FEBIP nanostructures was characterized by means of scanning electron microscopy (SEM) and atomic force microscopy (AFM). Local Auger electron spectroscopy (AES) was used for the chemical analysis of the deposits. The results are presented in a cumulative form; the full papers are attached in the Appendix.

A main theme of the thesis at hand is the fabrication of metal-containing nanostructures via FEBIP, i.e., gas assisted electron beam lithography techniques on top of organic or metal-organic films supported on different bulk substrates. In a second step the latter films were eventually cross-linked by electron irradiation and separated from the bulk support as ultrathin carbon nanomembranes (CNMs). In addition to the successful exploration of innovative techniques for the fabrication of nanostructured hybrid materials also fundamental electron induced processes within the molecular materials were investigated in detail with state-of-the-art surface science methods. In combination with the in depth characterization of the hybrid nanostructures a deeper understanding of the fabricated materials and the underlying processes could be achieved. The most important findings in this regard can be listed in a summarized form as follows:

- Metallic nanostructures can be fabricated with high purity on self-assembled monolayers (SAMs) via FEBIP in UHV.
- The SAMs can be transformed into CNMs via electron induced crosslinking, separated from their bulk substrate and transferred to other substrates.
- The FEBIP nanostructures remain intact after the transformation of SAMs into CNMs and are transferred to other substrates without significant modification.

- Physisorbed porphyrin layers prepared in vacuum can be also transformed into CNMs which considerably expands the possibility to prepare and functionalize CNMs.
- The EBISA process works successfully with $Fe(CO)_5$ on aromatic SAMs.
- The active species in the EBISA process on aromatic SAMs are deactivated within few hours.
- Copper nanoparticles can be ruled out as active species for the dissociation of $Fe(CO)_5$ during EBISA on HKUST-1.
- The cleavage of C-H bonds in the aromatic unit of organic species seems to play a crucial role in EBISA.

Overall, the methods explored in the thesis at hand are suitable to fabricate novel types of nanostructured hybrid materials. These are in particular metallic nanostructures on CNMs with high application potential. In addition, the finding that physisorbed porphyrins are well suitable as starting material for CNMs opens up new routes for the fabrication of membranes with specific functionalities. These hybrid materials need to be further characterized in future studies especially regarding their magnetic, thermal, optical and electric properties. The EBISA process and the chemical nature of electron irradiation of organic and metal-organic substrates were analyzed in detail. However, the exact mechanism could not be fully concluded and needs further investigation.

5 Zusammenfassung

In dieser Arbeit wurden funktionelle Hybridstrukturen bestehend aus metallischen Nanostrukturen (erzeugt mittels FEBIP) auf organischen oder metallorganischen Substraten hergestellt und analysiert. Darüber hinaus wurde eine detaillierte Untersuchung der elektroneninduzierten Chemie insbesondere während des EBISA-Prozesses für drei verschiedene Substrate vorgestellt. Die in dieser Arbeit analysierten Substrate sind SAMs bzw. CNMs bestehend aus TPT-Molekülen, dünne Schichten aus 2H-TPP-Molekülen und der SURMOF HKUST-1. Die FEBIP-Experimente wurden bei Raumtemperatur in einer UHV-Kammer durchgeführt. Die Morphologie der FEBIP Nanostrukturen wurde mittels Rasterelektronenmikroskopie (SEM) und Rasterkraftmikroskopie (AFM) untersucht. Lokale Augerelektronenspektroskopie (AES) wurde eingesetzt, um die chemische Zusammensetzung der Abscheidungen zu analysieren. Die Ergebnisse werden in einer kumulativen Form präsentiert. Die vollständigen Publikationen sind im Anhang beigefügt.

Ein Hauptthema der vorliegenden Arbeit ist die Herstellung von metallischen Nanostrukturen mittels FEBIP, d.h. gasunterstützter Elektronenstrahllithographie-Techniken auf organischen oder metallorganischen Filmen, die auf verschiedenen Bulk-Substraten aufgebracht sind. In einem zweiten Schritt wurden die letztgenannten Filme schließlich durch Elektronenbestrahlung vernetzt und als ultradünne Kohlenstoff-Nanomembranen (CNMs) vom Bulk-Träger getrennt. Neben der erfolgreichen Erforschung innovativer Techniken zur Herstellung nanostrukturierter Hybridmaterialien wurden auch grundlegende elektroneninduzierte Prozesse innerhalb der molekularen Ebene mit modernsten oberflächenwissenschaftlichen Methoden im Detail untersucht. In Kombination mit der eingehenden Charakterisierung der hybriden Nanostrukturen konnte so ein tieferes Verständnis der hergestellten Materialien und der zugrunde liegenden Prozesse erreicht werden. Die wichtigsten Erkenntnisse in diesem Zusammenhang lassen sich wie folgt zusammenfassend darstellen:

- Metallische Nanostrukturen können mit hoher Reinheit auf selbstorganisierenden Monolagen (SAMs) mittels FEBIP im UHV hergestellt werden.

- Die SAMs können durch elektroneninduzierte Vernetzung in CNMs umgewandelt, von ihrem Bulk-Substrat getrennt und auf andere Substrate übertragen werden.
- Die FEBIP-Nanostrukturen bleiben nach der Umwandlung der SAMs in CNMs intakt und werden ohne signifikante Veränderung auf andere Substrate übertragen.
- Physisorbierte Porphyrin-Schichten, die im Vakuum präpariert wurden, können ebenfalls in CNMs umgewandelt werden, was die Möglichkeiten zur Herstellung und Funktionalisierung von CNMs erheblich erweitert.
- Der EBISA-Prozess funktioniert erfolgreich mit $Fe(CO)_5$ auf aromatischen SAMs.
- Die aktiven Spezies im EBISA-Prozess auf aromatischen SAMs werden innerhalb weniger Stunden deaktiviert.
- Kupfernanopartikel können als aktive Spezies für die Dissoziation von $Fe(CO)_5$ während EBISA auf HKUST-1 ausgeschlossen werden.
- Die Spaltung von C-H-Bindungen in der aromatischen Einheit von organischen Spezies scheint eine entscheidende Rolle bei EBISA zu spielen.

Insgesamt sind die in der vorliegenden Arbeit untersuchten Methoden geeignet, neuartige nanostrukturierte Hybridmaterialien herzustellen. Diese sind insbesondere metallische Nanostrukturen auf CNMs mit hohem Anwendungspotenzial. Darüber hinaus eröffnet die Erkenntnis, dass sich physisorbierte Porphyrine gut als Ausgangsmaterial für CNMs eignen, neue Wege zur Herstellung von Membranen mit spezifischen Funktionalitäten. Diese Hybridmaterialien müssen in zukünftigen Studien weiter charakterisiert werden, insbesondere hinsichtlich ihrer magnetischen, thermischen, optischen und elektrischen Eigenschaften. Der EBISA-Prozess und die chemischen Prozesse der Elektronenbestrahlung von organischen und metall-organischen Substraten wurden im Detail analysiert. Der genaue Mechanismus konnte jedoch nicht vollständig geklärt werden und bedarf weiterer Analyse.

6 Literature

1. Moore, G. E., Cramming more components onto integrated circuits. McGraw-Hill New York, NY, USA: **1965**.

2. Marbach, H. Microscopic and Spectromicroscopic Insight and Fabrication of Nanoscaled Structures on Surfaces. FAU Erlangen-Nürnberg, **2010**.

3. van Dorp, W. F.; Hagen, C. W., A Critical Literature Review of Focused Electron Beam Induced Deposition. *J. Appl. Phys.* **2008,** *104* (8), 081301-42.

4. Utke, I.; Hoffmann, P.; Melngailis, J., Gas-assisted focused electron beam and ion beam processing and fabrication. *J. Vac. Sci. Technol.* **2008,** *26* (4).

5. Randolph, S. J.; Fowlkes, J. D.; Rack, P. D., Focused, Nanoscale Electron-Beam-Induced Deposition and Etching. *Crit. Rev. Solid State Mater. Sci.* **2006,** *31* (3), 55-89.

6. Silvis-Cividjian, N.; Hagen, C. W., Electron-Beam–Induced Nanometer-Scale Deposition. *Adv. Imaging Electron Phys.* **2006,** *143*, 1-235.

7. Marbach, H., Electron beam induced surface activation: a method for the lithographic fabrication of nanostructures via catalytic processes. *Appl. Phys. A: Mater. Sci. Process.* **2014,** (117), 987-995.

8. Walz, M.-M.; Schirmer, M.; Vollnhals, F.; Lukasczyk, T.; Steinrück, H.-P.; Marbach, H., Electrons as "Invisible Ink": Fabrication of Nanostructures by Local Electron Beam Induced Activation of SiOx. *Angew. Chem., Int. Ed.* **2010,** *49*, 4669-4673.

9. Walz, M.-M.; Vollnhals, F.; Rietzler, F.; Schirmer, M.; Steinrück, H.-P.; Marbach, H., Investigation of proximity effects in electron microscopy and lithography. *Appl. Phys. Lett.* **2012,** *100* (5), 053118.

10. Vollnhals, F.; Drost, M.; Tu, F.; Carrasco, E.; Späth, A.; Fink, R.; Steinrück, H.-P.; Marbach, H., Electron-beam induced deposition and autocatalytic decomposition of $Co(CO)_3NO$. *Beilstein J. Nanotechnol.* **2014,** *5*, 1175-1185.

11. Vollnhals, F.; Woolcot, T.; Walz, M.-M.; Seiler, S.; Steinrück, H.-P.; Thornton, G.; Marbach, H., Electron Beam-Induced Writing of Nanoscale Iron Wires on a Functional Metal Oxide. *J. Phys. Chem. C* **2013,** *117*, 17674-17679.

12. Lukasczyk, T.; Schirmer, M.; Steinrück, H. P.; Marbach, H., Electron-beam-induced deposition in ultrahigh vacuum: lithographic fabrication of clean iron nanostructures. *Small* **2008,** *4* (6), 841-846.

13. Schirmer, M.; Walz, M.-M.; Papp, C.; Kronast, F.; Gray, A. X.; Balke, B.; Cramm, S.; Fadley, C. S.; Steinrück, H.-P.; Marbach, H., Fabrication of layered nanostructures by successive electron beam induced deposition with two precursors: protective capping of metallic iron structures. *Nanotechnology* **2011,** *22*, 475304.

14. Walz, M.-M.; Vollnhals, F.; Schirmer, M.; Steinrück, H.-P.; Marbach, H., Generation of clean iron nanocrystals on an ultra-thin SiOx film on Si(001). *Phys. Chem. Chem. Phys.* **2011,** *13*, 17333-17338.

15. Drost, M.; Tu, F.; Berger, L.; Preischl, C.; Zhou, W.; Gliemann, H.; Wöll, C.; Marbach, H., Surface-Anchored Metal-Organic Frameworks as Versatile Resists for Gas-Assisted E-Beam Lithography: Fabrication of Sub-10 Nanometer Structures. *ACS Nano* **2018,** (12 (4)), 3825-3835.

16. Vollnhals, F.; Wintrich, P.; Walz, M.-M.; Steinrück, H.-P.; Marbach, H., Electron Beam Induced Surface Activation of Ultrathin Porphyrin Layers on Ag(111). *Langmuir* **2013,** *29*, 12290-12297.

17. Drost, M.; Tu, F.; Vollnhals, F.; Szenti, I.; Kiss, J.; Marbach, H., On the Principles of Tweeking Nanostructures Fabrication via Focused Electron Beam Induced Processing Combined with Catalytic Growth Processes. *Small Methods* **2017,** (1), 1700095.

18. Geyer, W.; Stadler, V.; Eck, W.; Zharnikov, M.; Gölzhäuser, A.; Grunze, M., Electron-induced crosslinking of aromatic self-assembled monolayers: Negative resists for nanolithography. *Appl. Phys. Lett.* **1999,** *75*, 2401-2403.

19. Zhang, X.; Neumann, C.; Angelova, P.; Beyer, A.; Gölzhäuser, A., Tailoring the Mechanics of Ultrathin Carbon Nanomembranes by Molecular Design. *Langmuir* **2014,** *30*, 8221-8227.

20. Turchanin, A.; El-Desawy, M.; Gölzhäuser, A., High thermal stability of cross-linked aromatic self-assembled monolayers: Nanopatterning via selective thermal desorption. *Appl. Phys. Lett.* **2007,** *90*, 053102.

21. Turchanin, A.; Beyer, A.; Nottbohm, C. T.; Zhang, X.; Stosch, R.; Sologubenko, A.; Mayer, J.; Hinze, P.; Weimann, T.; Gölzhäuser, A., One Nanometer Thin Carbon Nanosheets with Tunable Conductivity and Stiffness. *Adv. Mater.* **2009,** *21* (12), 1233-1237.

22. Ekinci, K. L.; Roukes, M. L., Nanoelectromechanical systems. *Rev. Sci. Instrum.* **2005,** *76* (6), 061101.

23. Butler, A. R.; Williams, D. L. H., The physiological role of nitric oxide. *Chem. Soc. Rev.* **1993,** *22* (4), 233-241.

24. Ford, P.; Bourassa, J.; Miranda, K.; Lee, B.; Lorkovic, I.; Boggs, S.; Kudo, S.; Laverman, L., Photochemistry of metal nitrosyl complexes. Delivery of nitric oxide to biological targets. *Coord. Chem. Rev.* **1998,** *171*, 185-202.

25. Paolesse, R.; Di Natale, C.; Dall'Orto, V. C.; Macagnano, A.; Angelaccio, A.; Motta, N.; Sgarlata, A.; Hurst, J.; Rezzano, I.; Mascini, M., Porphyrin thin films coated quartz crystal microbalances prepared by electropolymerization technique. *Thin Solid Films* **1999,** *354* (1-2), 245-250.

26. Rakow, N. A.; Suslick, K. S., A colorimetric sensor array for odour visualization. *Nature* **2000,** *406* (6797), 710-713.

27. Grätzel, M., Dye-sensitized solar cells. *J. Photochem. Photobiol., C* **2003,** *4* (2), 145-153.

28. Zucca, P.; Neves, C.; Simões, M. M.; Neves, M. d. G. P.; Cocco, G.; Sanjust, E., Immobilized lignin peroxidase-like metalloporphyrins as reusable catalysts in oxidative bleaching of industrial dyes. *Molecules* **2016,** *21* (7), 964.

29. Reimer, L., *Scanning electron microscopy: physics of image formation and microanalysis*. Springer-Verlag Berlin Heidelberg: **1998**.

30. Seiler, H., Einige aktuelle Probleme der Sekundarelektron-emission. *Z. angew. Phys.* **1967,** *22*, 249-263.

31. Everhart, T. E.; Thornley, R., Wide-band detector for micro-microampere low-energy electron currents. *J. Sci. Instrum.* **1960,** *37* (7), 246.

32. Brundle, C.; Watts, J.; Wolstenholme, J., X-ray photoelectron and Auger electron spectroscopy. *Analytical Instrumentation Handbook* **2004,** *399*.

33. Hesse, M.; Meier, H.; Zeeh, B., *Spektroskopische Methoden in der organischen Chemie*. Georg Thieme Verlag: **2005**.

34. Dawson, P. H., *Quadrupole mass spectrometry and its applications*. Elsevier: **2013**.

35. Binnig, G.; Quate, C. F.; Gerber, C., Atomic force microscope. *Phys. Rev. Lett.* **1986,** *56* (9), 930.

36. Hawkes, P. W.; Spence, J. C., *Science of microscopy*. Springer Science & Business Media: **2008**.

37. Oura, K.; Katayama, M.; Zotov, A.; Lifshits, V.; Saranin, A., *Surface Science - An Introduction*. Springer-Verlag: Berlin, **2003**.

38. Liu, L.; Xi, N.; Li, G.; Chen, H., *Nano Optoelectronic Sensors and Devices*. William Andrew Publishing: Oxford, **2012**.

39. Lukasczyk, T. Generation of pure iron nanostructures via electron-beam induced deposition in UHV. PhD Thesis, Friedrich-Alexander-Universität Erlangen-Nürnberg, Erlangen, **2010**.

40. Schirmer, M. Generation of Titanium Oxide Nanostructures via Electron Beam Induced Deposition in UHV. PhD Thesis, Friedrich-Alexander-Universität Erlangen-Nürnberg, Erlangen, **2012**.

41. Friedli, V.; Utke, I., Optimized molecule supply from nozzle-based gas injection systems for focused electron-and ion-beam induced deposition and etching: simulation and experiment. *J. Phys. D: Appl. Phys.* **2009,** *42* (12), 125305.

42. Love, J. C.; Estroff, L. A.; Kriebel, J. K.; Nuzzo, R. G.; Whitesides, G. M., Self-Assembled Monolayers of Thiolates on Metals as a Form of Nanotechnology. *Chem. Rev.* **2005,** *105* (4), 1103-1170.

43. Nuzzo, R. G.; Allara, D. L., Adsorption of bifunctional organic disulfides on gold surfaces. *J. Am. Chem. Soc.* **1983,** *105* (13), 4481-4483.

44. Dubois, L. H.; Zegarski, B. R.; Nuzzo, R. G., Molecular ordering of organosulfur compounds on Au (111) and Au (100): Adsorption from solution and in ultrahigh vacuum. *J. Chem. Phys.* **1993,** *98* (1), 678-688.

45. Dubois, L. H.; Nuzzo, R. G., Synthesis, structure, and properties of model organic surfaces. *Annu. Rev. Phys. Chem.* **1992,** *43* (1), 437-463.

46. Biebuyck, H. A.; Bain, C. D.; Whitesides, G. M., Comparison of organic monolayers on polycrystalline gold spontaneously assembled from solutions containing dialkyl disulfides or alkanethiols. *Langmuir* **1994,** *10* (6), 1825-1831.

47. Ishida, T.; Mizutani, W.; Azehara, H.; Sato, F.; Choi, N.; Akiba, U.; Fujihira, M.; Tokumoto, H., Adsorption Processes of Self-Assembled Monolayers Made from Terphenyl Thiols. *Langmuir* **2001,** *17* (24), 7459-7463.

48. Walczak, M. M.; Chung, C.; Stole, S. M.; Widrig, C. A.; Porter, M. D. J. J. o. t. A. C. s., Structure and interfacial properties of spontaneously adsorbed n-alkanethiolate monolayers on evaporated silver surfaces. **1991,** *113* (7), 2370-2378.

49. Fenter, P.; Eisenberger, P.; Li, J.; Camillone III, N.; Bernasek, S.; Scoles, G.; Ramanarayanan, T. A.; Liang, K., Structure of octadecyl thiol self-assembled on the silver (111) surface: an incommensurate monolayer. *Langmuir* **1991,** *7* (10), 2013-2016.

50. Laibinis, P. E.; Whitesides, G. M.; Allara, D. L.; Tao, Y. T.; Parikh, A. N.; Nuzzo, R. G., Comparison of the structures and wetting properties of self-assembled monolayers of n-alkanethiols on the coinage metal surfaces, copper, silver, and gold. *J. Am. Chem. Soc.* **1991,** *113* (19), 7152-7167.

51. Love, J. C.; Wolfe, D. B.; Haasch, R.; Chabinyc, M. L.; Paul, K. E.; Whitesides, G. M.; Nuzzo, R. G., Formation and structure of self-assembled monolayers of alkanethiolates on palladium. *J. Am. Chem. Soc.* **2003,** *125* (9), 2597-2609.

52. Carvalho, A.; Geissler, M.; Schmid, H.; Michel, B.; Delamarche, E., Self-assembled monolayers of eicosanethiol on palladium and their use in microcontact printing. *Langmuir* **2002,** *18* (6), 2406-2412.

53. Li, Z.; Chang, S.-C.; Williams, R. S., Self-assembly of alkanethiol molecules onto platinum and platinum oxide surfaces. *Langmuir* **2003,** *19* (17), 6744-6749.

54. Hutt, D. A.; Liu, C., Oxidation protection of copper surfaces using self-assembled monolayers of octadecanethiol. *Appl. Surf. Sci.* **2005,** *252* (2), 400-411.

55. Shekhah, O.; Wang, H.; Zacher, D.; Fischer, R. A.; Wöll, C., Growth mechanism of metal–organic frameworks: insights into the nucleation by employing a step-by-step route. *Angew. Chem., Int. Ed.* **2009,** *48* (27), 5038-5041.

56. Sushko, M. L.; Shluger, A. L., Rough and Fine Tuning of Metal Work Function via Chemisorbed Self-Assembled Monolayers. *Adv. Mater.* **2009,** *21* (10-11), 1111-1114.

57. Schön, J. H.; Meng, H.; Bao, Z., Self-assembled monolayer organic field-effect transistors. *Nature* **2001,** *413* (6857), 713-716.

58. Andringa, A.-M.; Spijkman, M.-J.; Smits, E. C.; Mathijssen, S. G.; van Hal, P. A.; Setayesh, S.; Willard, N. P.; Borshchev, O. V.; Ponomarenko, S. A.; Blom, P. W., Gas sensing with self-assembled monolayer field-effect transistors. *Org. Electron.* **2010,** *11* (5), 895-898.

59. Smits, E. C.; Mathijssen, S. G.; Van Hal, P. A.; Setayesh, S.; Geuns, T. C.; Mutsaers, K. A.; Cantatore, E.; Wondergem, H. J.; Werzer, O.; Resel, R., Bottom-up organic integrated circuits. *Nature* **2008,** *455* (7215), 956-959.

60. Ringk, A.; Roelofs, W. C.; Smits, E. C.; van der Marel, C.; Salzmann, I.; Neuhold, A.; Gelinck, G. H.; Resel, R.; De Leeuw, D. M.; Strohriegl, P., n-Type self-assembled monolayer field-effect transistors for flexible organic electronics. *Org. Electron.* **2013,** *14* (5), 1297-1304.

61. Yan, L.; Zhao, X.-M.; Whitesides, G. M., Patterning a preformed, reactive SAM using microcontact printing. *J. Am. Chem. Soc.* **1998,** *120* (24), 6179-6180.

62. Lahiri, J.; Ostuni, E.; Whitesides, G. M., Patterning ligands on reactive SAMs by microcontact printing. *Langmuir* **1999,** *15* (6), 2055-2060.

63. Shadnam, M. R.; Kirkwood, S. E.; Fedosejevs, R.; Amirfazli, A., Direct patterning of self-assembled monolayers on gold using a laser beam. *Langmuir* **2004,** *20* (7), 2667-2676.

64. Klauser, R.; Hong, I.-H.; Wang, S.-C.; Zharnikov, M.; Paul, A.; Gölzhäuser, A.; Terfort, A.; Chuang, T., Imaging and patterning of monomolecular resists by zone-plate-focused X-ray microprobe. *J. Phys. Chem. B* **2003,** *107* (47), 13133-13142.

65. Turchanin, A.; Schnietz, M.; El-Desawy, M.; Solak, H. H.; David, C.; Gölzhäuser, A., Fabrication of Molecular Nanotemplates in Self-Assembled Monolayers by Extreme-Ultraviolet-Induced Chemical Lithography. *Small* **2007,** *3*, 2114-2119.

66. Geyer, W.; Stadler, V.; Eck, W.; Gölzhäuser, A.; Grunze, M.; Sauer, M.; Weimann, T.; Hinze, P., Electron induced chemical nanolithography with self-assembled monolayers. *J. Vac. Sci. Technol. B* **2001,** *19* (6), 2732-2735.

67. Gölzhäuser, A.; Geyer, W.; Stadler, V.; Eck, W.; Grunze, M., Nanoscale patterning of self-assembled monolayers with electrons. *J. Vac. Sci. Technol. B* **2000,** *18* (6), 3414-3418.

68. Gölzhäuser, A.; Eck, W.; Geyer, W.; Stadler, V.; Weimann, T.; Hinze, P.; Grunze, M., Chemical nanolithography with electron beams. *Adv. Mater.* **2001,** *13* (11), 803-806.

69. Turchanin, A.; Käfer, D.; El-Desawy, M.; Wöll, C.; Witte, G.; Gölzhäuser, A., Molecular Mechanisms of Electron-Induced Cross-Linking in Aromatic SAMs. *Langmuir* **2009,** (25), 7342-7352.

70. Turchanin, A.; Gölzhäuser, A., Carbon Nanomembranes. *Adv. Mater.* **2016,** *28*, 6075-6103.

71. Angelova, P.; Vieker, H.; Weber, N. E.; Matei, D.; Reimer, O.; Meier, I.; Kurasch, S.; Biskupek, J.; Lorbach, D.; Wunderlich, K.; Chen, L.; Terfort, A.; Klapper, M.; Müllen, K.; Kaiser, U.; Gölzhäuser, A.; Turchanin, A., A Universal Scheme to Convert Aromatic Molecular Monolayers into Functional Carbon Nanomembranes. *ACS Nano* **2013,** *7*, 6489.

72. Yang, Y.; Dementyev, P.; Biere, N.; Emmrich, D.; Stohmann, P.; Korzetz, R.; Zhang, X.; Beyer, A.; Koch, S.; Anselmetti, D.; Gölzhäuser, A., Rapid Water Permeation Through Carbon Nanomembranes with Sub-Nanometer Channels. *ACS Nano* **2018,** *12* (5), 4695-4701.

73. Beyer, A.; Turchanin, A.; Nottbohm, C. T.; Mellech, N.; Schnietz, M.; Gölzhäuser, A., Fabrication of metal patterns on freestanding graphenoid nanomembranes. *J. Vac. Sci. Technol. B* **2010,** *28* (6), C6D5-C6D10.

74. Sirmaci, Y. D.; Tang, Z.; Fasold, S.; Neumann, C.; Pertsch, T.; Turchanin, A.; Staude, I., Plasmonic Metasurfaces Situated on Ultrathin Carbon Nanomembranes. *ACS Photonics* **2020,** *7* (4), 1060-1066.

75. Milgrom, L. R., *The colours of life: an introduction to the chemistry of porphyrins and related compounds*. Oxforf University Press: **1997**.

76. Darwent, J. R.; Douglas, P.; Harriman, A.; Porter, G.; Richoux, M.-C., Metal phthalocyanines and porphyrins as photosensitizers for reduction of water to hydrogen. *Coord. Chem. Rev.* **1982,** *44* (1), 83-126.

77. Gottfried, J. M., Surface chemistry of porphyrins and phthalocyanines. *Surf. Sci. Rep.* **2015,** *70* (3), 259-379.

78. Auwarter, W.; Ecija, D.; Klappenberger, F.; Barth, J., Porphyrins at Interfaces. . *Nat. Chem.* **2015,** *7*, 105-120.

79. Ruggieri, C.; Rangan, S.; Bartynski, R. A.; Galoppini, E., Zinc(II)tetraphenylporphyrin on Ag(100) and Ag(111): Multilayer desorption and dehydrogenation. *J. Phys. Chem. C* **2016,** *120* (14), 7575-7585.

80. Yokoyama, T.; Yokoyama, S.; Kamikado, T.; Mashiko, S., Nonplanar adsorption and orientational ordering of porphyrin molecules on Au (111). *J. Chem. Phys.* **2001,** *115* (8), 3814-3818.

81. Kitagawa, S.; Kitaura, R.; Noro, S. i., Functional porous coordination polymers. *Angew. Chem., Int. Ed.* **2004,** *43* (18), 2334-2375.

82. Rowsell, J. L.; Yaghi, O. M., Metal–organic frameworks: a new class of porous materials. *Microporous Mesoporous Mat.* **2004,** *73* (1-2), 3-14.

83. Gliemann, H.; Wöll, C., Epitaxially grown metal-organic frameworks. *Mater. Today* **2012,** *15* (3), 110-116.

84. Hoskins, B. F.; Robson, R., Design and construction of a new class of scaffolding-like materials comprising infinite polymeric frameworks of 3D-linked molecular rods. A reappraisal of the zinc cyanide and cadmium cyanide structures and the synthesis and structure of the diamond-related frameworks $[N(CH_3)_4][CuIZnII(CN)_4]$ and CuI [4, 4', 4'', 4'''-tetracyanotetraphenylmethane] $BF_4 \cdot xC_6H_5NO_2$. *J. Am. Chem. Soc.* **1990,** *112* (4), 1546-1554.

85. Rowsell, J. L.; Yaghi, O. M., Metal–organic frameworks: a new class of porous materials. *Microporous Mesoporous Mat.* **2004,** *73* (1-2), 3-14.

86. Horcajada, P.; Serre, C.; Maurin, G.; Ramsahye, N. A.; Balas, F.; Vallet-Regi, M.; Sebban, M.; Taulelle, F.; Férey, G., Flexible porous metal-organic frameworks for a controlled drug delivery. *J. Am. Chem. Soc.* **2008,** *130* (21), 6774-6780.

87. Horcajada, P.; Serre, C.; Vallet-Regí, M.; Sebban, M.; Taulelle, F.; Férey, G., Metal–organic frameworks as efficient materials for drug delivery. *Angew. Chem., Int. Ed.* **2006,** *118* (36), 6120-6124.

88. Snurr, R. Q.; Hupp, J. T.; Nguyen, S. T., Prospects for nanoporous metal-organic materials in advanced separations processes. *AICHE J.* **2004,** *50* (6), 1090-1095.

89. Maji, T. K.; Uemura, K.; Chang, H. C.; Matsuda, R.; Kitagawa, S., Expanding and Shrinking Porous Modulation Based on Pillared-Layer Coordination Polymers Showing Selective Guest Adsorption. *Angew. Chem., Int. Ed.* **2004,** *116* (25), 3331-3334.

90. Hermes, S.; Schröder, F.; Amirjalayer, S.; Schmid, R.; Fischer, R. A., Loading of porous metal–organic open frameworks with organometallic CVD precursors: inclusion compounds of the type $[L_nM]_a$ @ MOF-5. *J. Mater. Chem.* **2006,** *16* (25), 2464-2472.

91. Hermes, S.; Schröter, M. K.; Schmid, R.; Khodeir, L.; Muhler, M.; Tissler, A.; Fischer, R. W.; Fischer, R. A., Metal@ MOF: loading of highly porous coordination polymers host lattices by metal organic chemical vapor deposition. *Angew. Chem., Int. Ed.* **2005,** *44* (38), 6237-6241.

92. Allendorf, M. D.; Houk, R. J.; Andruszkiewicz, L.; Talin, A. A.; Pikarsky, J.; Choudhury, A.; Gall, K. A.; Hesketh, P. J., Stress-induced chemical detection using flexible metal− organic frameworks. *J. Am. Chem. Soc.* **2008,** *130* (44), 14404-14405.

93. Chui, S. S. Y.; Lo, S. M. F.; Charmant, J. P. H.; Orpen, A. G.; Williams, I. D., A Chemically Functionalizable Nanoporous Material $[Cu_3(TMA)_2(H_2O)_3]$. *Science* **1999,** *283* (5405), 1148.

94. Stewart, R. L., Insulating films formed under electron and ion bombardment. *Phys. Rev.* **1934,** *45* (7), 488.

95. Baker, A. G.; Morris, W. C., Deposition of metallic films by electron impact decomposition of organometallic vapors. *Rev. Sci. Instrum.* **1961,** *32* (4), 458-458.

96. Silvis-Cividjian, N.; Hagen, C.; Kruit, P., Spatial resolution limits in electron-beam-induced deposition. *J. Appl. Phys.* **2005,** *98* (8), 084905.

97. Song, M.; Furuya, K., Fabrication and characterization of nanostructures on insulator substrates by electron-beam-induced deposition. *Sci. Technol. Adv. Mat.* **2008,** *9*, 023002.

98. Winkler, R.; Fowlkes, J. D.; Rack, P. D.; Plank, H., 3D nanoprinting via focused electron beams. *J. Appl. Phys.* **2019,** *125* (21), 210901.

99. Fowlkes, J. D.; Winkler, R.; Lewis, B. B.; Stanford, M. G.; Plank, H.; Rack, P. D., Simulation-guided 3D nanomanufacturing via focused electron beam induced deposition. *ACS nano* **2016,** *10* (6), 6163-6172.

100. Qian, W.; Nguyen, C.; Turner, J. A.; Liu, D. J. M., Electron-Beam-Induced Deposition of Carbon Nanorod via Spot Mode as Highly Stable and Sensitive AFM Probe Tip. *Microsc. Microanal.* **2017,** *23* (S1), 1736-1737.

101. Qian, W.; Sun, S.; Song, J.; Nguyen, C.; Ducharme, S.; Turner, J. A., Focused electron-beam-induced deposition for fabrication of highly durable and sensitive metallic AFM-IR probes. *Nanotechnology* **2018,** *29* (33), 335702.

102. Murakami, K.; Wakaya, F.; Takai, M., Observation of fringelike electron-emission pattern in field emission from Pt field emitter fabricated by electron-beam-induced deposition. *J. Vac. Sci. Technol. B* **2007,** *25* (4), 1310-1314.

103. Tsukatani, Y.; Yamasaki, N.; Murakami, K.; Wakaya, F.; Takai, M., Transport properties of Pt nanowires fabricated by beam-induced deposition. *Jpn. J. Appl. Phys.* **2005,** *44* (7S), 5683.

104. Edinger, K.; Becht, H.; Bihr, J.; Boegli, V.; Budach, M.; Hofmann, T.; Koops, H. W.; Kuschnerus, P.; Oster, J.; Spies, P., Electron-beam-based photomask repair. *J. Vac. Sci. Technol. B* **2004,** *22* (6), 2902-2906.

105. Liang, T.; Frendberg, E.; Lieberman, B.; Stivers, A., Advanced photolithographic mask repair using electron beams. *J. Vac. Sci. Technol. B* **2005,** *23* (6), 3101-3105.

106. Botman, A.; Mulders, J. J. L.; Hagen, C. W., Creating pure nanostructures from electron-beam-induced deposition using purification techniques: a technology perspective *Nanotechnology* **2009,** *20* (372001), 1-17.

107. Fernández-Pacheco, A.; De Teresa, J.; Córdoba, R.; Ibarra, M. R., Magnetotransport properties of high-quality cobalt nanowires grown by focused-electron-beam-induced deposition. *J. Phys. D: Appl. Phys.* **2009,** *42* (5), 055005.

108. Berger, L.; Madajska, K.; Szymanska, I. B.; Höflich, K.; Polyakov, M. N.; Jurczyk, J.; Guerra-Nuñez, C.; Utke, I., Gas-assisted silver deposition with a focused electron beam. *Beilstein J Nanotechnol.* **2018,** *9* (1), 224-232.

109. Belić, D.; Shawrav, M. M.; Gavagnin, M.; Stöger-Pollach, M.; Wanzenboeck, H. D.; Bertagnolli, E., Direct-write deposition and focused-electron-beam-induced purification of gold nanostructures. *ACS Appl. Mater. Interfaces* **2015,** *7* (4), 2467-2479.

110. Begun, E.; Dobrovolskiy, O. V.; Kompaniiets, M.; Sachser, R.; Gspan, C.; Plank, H.; Huth, M., Post-growth purification of Co nanostructures prepared by focused electron beam induced deposition. *Nanotechnology* **2015,** *26* (7), 075301.

111. Lewis, B. B.; Stanford, M. G.; Fowlkes, J. D.; Lester, K.; Plank, H.; Rack, P. D., Electron-stimulated purification of platinum nanostructures grown via focused electron beam induced deposition. *Beilstein J Nanotechnol.* **2015,** *6* (1), 907-918.

112. Szkudlarek, A.; Vaz, A. R.; Zhang, Y.; Rudkowski, A.; Kapusta, C.; Erni, R.; Moshkalev, S.; Utke, I., Formation of pure Cu nanocrystals upon post-growth annealing of Cu–C material obtained from focused electron beam induced deposition: comparison of different methods. *Beilstein J Nanotechnol.* **2015,** *6* (1), 1508-1517.

113. Villamor, E.; Casanova, F.; Trompenaars, P.; Mulders, J., Embedded purification for electron beam induced Pt deposition using $MeCpPtMe_3$. *Nanotechnology* **2015,** *26* (9), 095303.

114. Stanford, M. G.; Lewis, B. B.; Noh, J. H.; Fowlkes, J. D.; Rack, P. D., Inert gas enhanced laser-assisted purification of platinum electron-beam-induced deposits. *ACS Appl. Mater. Interfaces* **2015,** *7* (35), 19579-19588.

115. Shawrav, M. M.; Taus, P.; Wanzenboeck, H. D.; Schinnerl, M.; Stöger-Pollach, M.; Schwarz, S.; Steiger-Thirsfeld, A.; Bertagnolli, E., Highly conductive and pure gold nanostructures grown by electron beam induced deposition. *Sci. Rep.* **2016,** *6*, 34003.

116. Van Dorp, W. F.; Van Someren, B.; Hagen, C. W.; Kruit, P.; Crozier, P. A., Approaching the resolution limit of nanometer-scale electron beam-induced deposition. *Nano Lett.* **2005,** *5* (7), 1303-1307.

117. Böhler, E.; Warneke, J.; Swiderek, P., Control of chemical reactions and synthesis by low-energy electrons. *Chem. Soc. Rev.* **2013,** *42* (24), 9219-9231.

118. Thorman, R. M.; Jensen, P. A.; Yu, J.-C.; Matsuda, S. J.; McElwee-White, L.; Ingólfsson, O.; Fairbrother, D. H., Electron-Induced Reactions of $Ru(CO)_4I_2$: Gas Phase, Surface, and Electron Beam-Induced Deposition. *J. Phys. Chem. C* **2020,** *124* (19), 10593-10604.

119. Kondo, Y.; Ishikawa, K.; Hayashi, T. In *Electron induced reactions in gas phase $MeCpPtMe_3$ and $Pd(hfac)_2$*, J. Phys.: Conf. Ser., **2012**; 052019.

120. TP, R. K.; Hari, S.; Damodaran, K. K.; Ingólfsson, O.; Hagen, C. W., Electron beam induced deposition of silacyclohexane and dichlorosilacyclohexane: the role of dissociative ionization and dissociative electron attachment in the deposition process. *Beilstein J Nanotechnol.* **2017,** *8* (1), 2376-2388.

121. Wnuk, J. D.; Gorham, J. M.; Rosenberg, S. G.; van Dorp, W. F.; Madey, T. E.; Hagen, C. W.; Fairbrother, D. H., Electron induced surface reactions of the organometallic precursor trimethyl (methylcyclopentadienyl) platinum (IV). *J. Phys. Chem. C* **2009,** *113* (6), 2487-2496.

122. Wnuk, J. D.; Gorham, J. M.; Rosenberg, S. G.; van Dorp, W. F.; Madey, T. E.; Hagen, C. W.; Fairbrother, D. H., Electron beam irradiation of dimethyl-(acetylacetonate) gold (III) adsorbed onto solid substrates. *J. Appl. Phys.* **2010,** *107* (5), 054301.

123. Rosenberg, S. G.; Barclay, M.; Fairbrother, D. H., Electron induced reactions of surface adsorbed tungsten hexacarbonyl ($W(CO)_6$). *Phys. Chem. Chem. Phys.* **2013,** *15* (11), 4002-4015.

124. Rosenberg, S. G.; Barclay, M.; Fairbrother, D. H., Electron beam induced reactions of adsorbed cobalt tricarbonyl nitrosyl ($Co(CO)_3NO$) molecules. *J. Phys. Chem. C* **2013,** *117* (31), 16053-16064.

125. Rosenberg, S. G.; Barclay, M.; Fairbrother, D. H., Electron induced surface reactions of organometallic metal $(hfac)_2$ precursors and deposit purification. *ACS Appl. Mater. Interfaces* **2014,** *6* (11), 8590-8601.

126. Spencer, J. A.; Rosenberg, S. G.; Barclay, M.; Wu, Y.-C.; McElwee-White, L.; Fairbrother, D. H., Understanding the electron-stimulated surface reactions of organometallic complexes to enable design of precursors for electron beam-induced deposition. *J. Appl. Phys. A* **2014,** *117* (4), 1631-1644.

127. Spencer, J. A.; Brannaka, J. A.; Barclay, M.; McElwee-White, L.; Fairbrother, D. H., Electron-induced surface reactions of η^3-Allyl ruthenium tricarbonyl bromide [$(\eta^3\text{-}C_3H_5)Ru(CO)_3Br$]: contrasting the Behavior of Different Ligands. *J. Phys. Chem. C* **2015,** *119* (27), 15349-15359.

128. Walz, M.; Vollnhals, F.; Rietzler, F.; Schirmer, M.; Kunzmann, A.; Steinrück, H.; Marbach, H., Thin membranes versus bulk substrates: investigation of proximity effects in focused electron beam-induced processing. *J. Phys. D: Appl. Phys.* **2012,** *45* (22), 225306.

129. Muthukumar, K.; Jeschke, H. O.; Valentí, R.; Begun, E.; Schwenk, J.; Porrati, F.; Huth, M., Spontaneous dissociation of $Co_2(CO)_8$ and autocatalytic growth of Co on SiO_2: A combined experimental and theoretical investigation. *Beilstein J. Nanotechnol.* **2012,** *3* (1), 546-555.

130. Knotek, M.; Feibelman, P. J., Ion desorption by core-hole Auger decay. *Phys. Rev. Lett.* **1978,** *40* (14), 964.

131. Niehus, H.; Losch, W., ESD on metal oxides and oxygen adsorption layers: Evidence for different mechanisms in electron stimulated desorption. *Surf. Sci.* **1981,** *111* (2), 344-350.

132. Balaur, E.; Djenizian, T.; Boukherroub, R.; Chazalviel, J.; Ozanam, F.; Schmuki, P., Electron beam-induced modification of organic monolayers on Si(111) surfaces used for selective electrodeposition. *Electrochem. Commun.* **2004,** *6* (2), 153-157.

133. Wedler, G., *Lehrbuch der Physikalischen Chemie*. Wiley-VCH Verlag GmbH: **2004**.

134. Zaera, F., Mechanism for the decomposition of iron pentacarbonyl on Pt (111): evidence for iron tetracarbonyl and iron tricarbonyl intermediates. *Surf. Sci.* **1991,** *255* (3), 280-288.

135. Lukasczyk, T.; Schirmer, M.; Steinrück, H.-P.; Marbach, H., Generation of clean iron structures by electron-beam-induced deposition and selective catalytic decomposition of iron pentacarbonyl on Rh (110). *Langmuir* **2009,** *25* (19), 11930-11939.

136. Kunz, R.; Allen, T.; Mayer, T., Selective area deposition of metals using low-energy electron beams. *J. Vac. Sci. Technol. B* **1987,** *5* (5), 1427-1431.

137. Kunz, R.; Mayer, T., Catalytic growth rate enhancement of electron beam deposited iron films. *Appl. Phys. Lett.* **1987,** *50* (15), 962-964.

138. Tu, F. On the Lithographic Fabrication of Fe and Co Nanostructures via Focused Electron/Photon Beam Induced Processing: Properties and Applications of the Structures. PhD Thesis, FAU Erlangen-Nürnberg, **2017**.

139. Drost, M. Investigating Focused Electron Beam Induced Processing on Organic and Metal-Organic Substrates. PhD Thesis, FAU Erlangen-Nürnberg, **2017**.

140. Winter, A.; George, A.; Neumann, C.; Tang, Z.; Mohn, M. J.; Biskupek, J.; Masurkar, N.; Reddy, A. L. M.; Weimann, T.; Hübner, U.; Kaiser, U.; Turchanin, A., Lateral heterostructures of two-dimensional materials by electron-beam induced stitching. *Carbon* **2018,** *128*, 106-116.

141. Dementyev, P.; Naberezhnyi, D.; Westphal, M.; Buck, M.; Gölzhäuser, A., Carbon Nanomembranes from Aromatic Carboxylate Precursors. *ChemPhysChem* **2020,** *21* (10), 1006-1011.

142. Neumann, C.; Szwed, M.; Frey, M.; Tang, Z.; Kozieł, K.; Cyganik, P.; Turchanin, A., Preparation of Carbon Nanomembranes without Chemically Active Groups. *ACS Appl. Mater. Interfaces* **2019,** *11* (34), 31176-31181.

143. Aagaard, N. D.; Azcárate, J. C.; Olmos-Asar, J.; Mariscal, M. M.; Solla-Gullón, J.; Zelaya, E.; Fonticelli, M. H., Mechanistic Framework for the Formation of Different Sulfur Species by Electron Irradiation of n-Dodecanethiol Self-Assembled Monolayers on Au(111) and Au(100). *J. Phys. Chem. C* **2020,** *124* (41), 22591-22600.

144. Neumann, C.; Wilhelm, R.; Küllmer, M.; Turchanin, A., Low-energy electron irradiation induced synthesis of molecular nanosheets: An influence of the electron beam energy. *Faraday Discuss.* **2020**.

145. Jacobs, B. W.; Houk, R. J.; Wong, B. M.; Talin, A. A.; Allendorf, M. D., Electron beam synthesis of metal and semiconductor nanoparticles using metal–organic frameworks as ordered precursors. *Nanotechnology* **2011,** *22* (37), 375601.

146. Rückriem, K.; Grotheer, S.; Vieker, H.; Penner, P.; Beyer, A.; Gölzhäuser, A.; Swiderek, P., Efficient electron-induced removal of oxalate ions and formation of copper nanoparticles from copper (II) oxalate precursor layers. *Beilstein J Nanotechnol.* **2016,** *7* (1), 852-861.

7 Abbreviations

2D	Two-Dimensional
2H-TPP	5,10,15,20-Tetraphenylporphyrin
3D	Three-Dimensional
AE	Auger Electron
AES	Auger Electron Spectroscopy
AFM	Atomic Force Microscopy
AG	Autocatalytic Growth
BSE	Backscattered Electron
btc	Benzene-1,3,5-tricarboxylate
CNM	Carbon Nanomembrane
DEA	Dissociative Electron Attachment
DI	Dissociative Ionization
EBID	Electron Beam Induced Deposition
EBIE	Electron Beam Induced Etching
EBISA	Electron Beam Induced Surface Activation
EBL	Electron Beam Lithography
EI	Electron Impact
E_{kin}	Kinetic Energy
ESD	Electron Stimulated Desorption
EUV	Extreme UltraViolet
FEBIP	Focused Electron Beam Induced Processing
FSE	Forward Scattered Electron

Abbreviations

HKUST-1	Copper benzene-1,3,5-tricarboxylate
HV	High Vacuum
MOF	Metal-Organic Framework
ND	Neutral Dissociation
NEMS	Nanoelectromechanical Systems
NEXAFS	Near Edge X-ray Absorption Fine Structure Spectroscopy
PE	Primary Electron
PMMA	Poly(methyl methacrylate)
QMS	Quadrupole Mass Spectrometry
RAIRS	Reflection Absorption Infrared Spectroscopy
RT	Room Temperature
SAM	Self-Assembled Monolayer
SE	Secondary Electron
SEM	Scanning Electron Microscopy
STM	Scanning Transmission Microscopy
STXM	Scanning Transmission X-ray microscopy
SURMOF	Surface-Anchored Metal-Organic Framework
TEM	Transmission Electron Microscopy
TPT	Terphenylthiol
UHV	Ultra-High Vacuum
UV	UltraViolet
Z	Atomic Number

8 Acknowledgement

The thesis at hand would have certainly been not possible without the support and help of a lot of people. I want to express my gratitude to:

PD Dr. Hubertus Marbach for excellent supervision and support on both scientific and personal level during my PhD time.

Professor Hans-Peter Steinrück for giving me the opportunity to do my PhD at his chair and providing outstanding scientific as well as social environment.

My colleagues from the FEBIP lab, Elif Bilgilisoy, Dr. Florian Vollnhals, Dr. Fan Tu, Dr. Martin Drost and Alexander Wolfram. Thank you for creating such an excellent working atmosphere. I really enjoyed working with you!

My collaboration partners from the University of Bremen, Professor Petra Swiderek, Dr. Kai Ahlenhoff, Markus Rohdenburg and René Cartaya. Thank you for the pleasant stay at the University of Bremen and the successful scientific collaboration.

My collaboration partners from the University of Bielefeld, Professor Armin Gölzhäuser and Linh Le Hoang. It was a pleasure working with you.

Hans-Peter Bäumler, Bernd Kress, Friedhold Wölfel and all the members of the mechanical workshop for their dedicated technical support as well as building or repairing various devices enabling outstanding experimental working conditions.

Besides my colleagues, I want to thank my parents and sisters and especially my partner Ramona for their continuous and unlimited support.

9 Appendix

[P1] Controlled Electron-Induced Fabrication of Metallic Nanostructures on 1nm Thick Membranes

C. Preischl, L. H. Le, E. Bilgilisoy, F. Vollnhals, A. Gölzhäuser, H. Marbach

Small **2020**, *16*, 2003947; DOI: 10.1002/smll.202003947

The author´s contribution is the performance and interpretation of the EBID, AES, SAM, AFM and transfer experiments. The manuscript was prepared by the author.

[P2] Exploring the Fabrication and Transfer Mechanism of Metallic Nanostructures on Carbon Nanomembranes via Focused Electron Beam Induced Processing

C. Preischl, L. H. Le, E. Bilgilisoy, A. Gölzhäuser, H. Marbach

Beilstein J. Nanotechnol. **2021**, *12*, 319-329; DOI: 10.3762/bjnano.12.26

The author´s contribution is the performance and interpretation of the EBID, EBISA, AES, AFM and transfer experiments. The manuscript was prepared by the author.

[P3] Ultrathin Carbon Nanomembranes from 5,10,15,20-Tetraphenylporphyrin: Electron Beam Induced Fabrication and Functionalization via Focused Electron Beam Induced Processing

C. Preischl, M. Rohdenburg, E. Bilgilisoy, R. Cartaya, P. Swiderek, H. Marbach

J. Phys. Chem. C. **2020**, *124*, 28335-28344; DOI: 10.1021/acs.jpcc.0c09694

The author´s contribution is the performance and interpretation of the EBID, EBISA, AES and transfer experiments. The RAIRS and ESD data were acquired and analyzed together with M. Rohdenburg and R. Cartaya during a two-week research stay at the University Bremen. The manuscript was prepared by the author.

[P4] Electron Beam-Induced Surface Activation of Metal-Organic Framework HKUST-1: Unravelling the Underlying Chemistry

K. Ahlenhoff, **C. Preischl**, P. Swiderek, H. Marbach

J. Phys. Chem. C **2018**, *122*, 26658-26670; DOI: 10.1021/acs.jpcc.8b06226

The author´s contribution is the performance and interpretation of the EBID, EBISA and AES experiments. The manuscript was prepared in close cooperation by all authors.